ORIGINAL ARTICLE

Quasi-X-braced steel moment frames (QXB-MFs) evaluation using analytical and numerical methods

Nader Fanaie[1] · Alireza Shirpour[1]

Abstract

Typical concentrically braced frames (CBFs), such as cross-braced (X-braced) frames, are commonly used to provide resistance against lateral loads. These systems are prone to buckling under compression, resulting in instability before reaching the yield strength. In other words, this bracing system exhibits an asymmetric behavior in tension and compression that undermines its energy dissipation capacity during excitation and leads to substantial damage to the structural and non-structural members. In an attempt to improve these shortcomings, this study introduces the novel quasi-X-braced frames. The stiffness and stability of the quasi-X-braced steel moment frames were evaluated by novel analytical and numerical methods. Drawing on strain energy concepts and Castigliano's theorem, this study presents an accurate analytical formulation for the lateral elastic stiffness of two-dimensional single-span and one-story quasi-X-braced steel moment frames (QXB-MFs). In this regard, all effective parameters, including the axial and shear loads and bending moments of all members, were taken into account. The proposed relation was validated with results from different cases using OpenSees. The error between the elastic stiffness results of the developed relation and the finite element numerical analysis was found to be negligible. Also, the seismic performance of QXB-MF systems was investigated according to the FEMA P695 methodology for near-field and far-field ground motion records compared with the intermediate moment frame. The results showed that using quasi-X braces in the intermediate moment frame improves the seismic performance of this system.

Keywords Steel moment frame · Quasi-X brace · Castigliano's theorem · Strain energy · Elastic lateral stiffness · Incremental dynamic analysis (IDA) · Near-field and far-field ground motion records

✉ Nader Fanaie
  fanaie@kntu.ac.ir

  Alireza Shirpour
  alireza.shirpour@email.kntu.ac.ir

1   Department of Civil Engineering, K. N. Toosi University of Technology, No. 1346, Vali-Asr Street, P.O. Box. 15875-4416, Tehran 19697, Iran
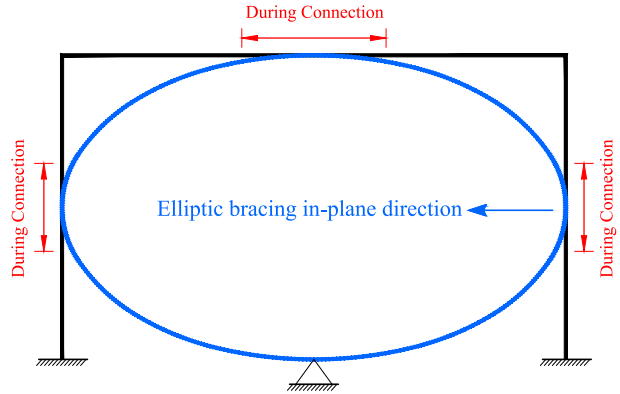
1 Introduction

Before the 1994 Northridge earthquake, steel moment frame structures were advertised for their flexibility and resistance to earthquakes compared to other common types of structures. This seismic event ravaged steel moment-resisting frames with welded beam-to-column connections. Considerable restoration costs and the broad damage distribution in the system prompted changes in regulations on steel structures around the world. At that point, structural systems with lateral-resisting members attracted designers. Damage was confined to specific members in these systems, which drastically reduced repair costs. The concentrically braced frame (CBF) is an example of these systems where the bracing component serves as a sacrificial fuse. These systems show impressive strength and stiffness against cyclic lateral loads but offer poor flexibility and energy capacity as the bracing buckles under compression. Moreover, due to the considerable difference of tensile and compressive strengths, the cross-braced beams, columns, and beam-to-column connections are faced with considerable demands, raising the construction cost. In this light, the seismic behavior of these bracing systems and solutions to improve it has been the subject of extensive research (Ebadi and Sabouri-Ghomi 2012; Grande and Rasulo 2013; Fanaie et al. 2017; Mahmoudi et al. 2018; Moradi Garoosi et al. 2018; Kumar et al. 2019; Sen et al. 2019; Roeder et al. 2020). Previous studies on improving the behavior of CBFs can be divided into two groups. The first group of studies proposes using buckling-restrained braces (BRBs). This option was developed to correct the bracing systems and make their compressive and tensile behavior more compatible (Fanaie and Dizaj 2014; Afsar Dizaj et al. 2018; Kachooee and Kafi 2018). The second group of studies, to which the present study belongs, advocate using sacrificial fuses in specific parts on the bracing or its connections to concentrate the damage and prevent damage in other main components (Dussault 2012; Arzeytoon and Toufigh 2018; Cheraghi and Zahrai 2019; Mahmoudi et al. 2019; Shirinkam and Razzaghi 2020; Varughese and El-Hacha 2020; Fanaie and Shirpour 2023).

In 1995, Moghaddam and Estekanchi introduced the Off-center Bracing System (OBS) to improve CBFs. The system includes an indirect bracing system with specific eccentricity. The mid-point of this element is connected to the corner of the frame by another member, with all three working under tension when the system is laterally loaded (Moghaddam and Estekanchi 1995, 1999). Recently, Bazzaz et al. thoroughly studied this structural system. One of their studies investigated some numerical frame models with optimum eccentricity in OBS and a circular element at the end. It was shown that placing ductile circular elements on the end of the OBS increases the system's ductility and energy dissipation (Andalib et al. 2014; Bazzaz et al. 2014, 2015a, b). In 2016, capitalizing on bending steel plates for energy dissipation, Payandehjoo et al. introduced the drawer bracing system (DBS) to improve the seismic performance of cross-braced frames. The DBS comprises three parallel plates connected by transfer plates. By converting axial loads to bending moment in transfer plates, the parallel plates prevent local buckling in the bracing and improve the energy dissipation and flexibility of cross-bracing systems by eliminating buckling (Payandehjoo et al. 2016; Payandehjoo and Ghasemzadeh 2017). In the same year, Jouneghani et al. introduced a new elliptic brace (Fig. 1).

Besides improving the structural behavior and higher energy dissipation in the structural system, this bracing system does not face architectural space limitations to place openings. One of the biggest problems with this brace is that bracing members are connected to columns. The reason is that incorrect implementation, and large shear exerted by the bracing on the column assist plastic hinge formation in the middle of the column (Jouneghani

**Fig. 1** Frame with elliptic bracing (Jouneghani et al. 2016)

et al. 2016, 2020; Jouneghani and Haghollahi 2020). In 2019, Taiyari et al. introduced a novel energy dissipation system that relied on U-shaped steel strips in the bracing. This damper worked by dissipating the earthquake's energy input using U-shaped steel strips. The straight parts of the U-shaped elements made the biggest contribution to the deformation capacity of the damper, which could be controlled by changing the lengths of different parts. The results of tests on the specimens showed a high energy dissipation capacity (Taiyari et al. 2019). In the same year, Ismail introduced a new elastoplastic bracing system (Fig. 2).

The system comprised a deforming steel ring at the center and four steel arcs on the sides that stayed tangent to the central ring and their adjacent arc and were connected to the corner of the frame directly or by a rigid arm. This study investigated the capacity of the brace to control structural vibrations and other vibration-dependent responses by numerical study under realistic and artificial dynamic excitation. It was shown that by effectively reducing and controlling structural vibrations at a low cost, this brace could be a cost-effective substitute for conventional bracing systems (Ismail 2019).

In 1969, Lee presented the 12×12 stiffness matrix of a curved beam using 3×3 matrix subsets and considering the Castigliano's theorem. His calculations did not account for the effects of axial loads and transverse shear (Lee 1969). In 1971, Rao developed the differential

Fig. 2 Elevation view of the AR-Brace (Ismail 2019)
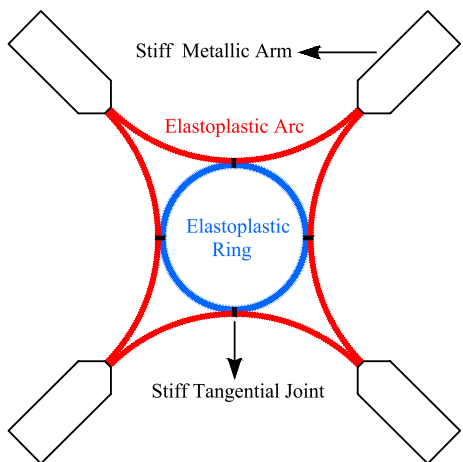
equations for the vibrations of a curved beam in bending and torsion using Hamilton's principle (Rao 1971). In 1972, Davis et al. obtained the stiffness matrix of a finite element using load–displacement curves. The relations were based on the differential equations of a small component in static equilibrium. Both Rao and Davis considered the effects of transverse shear deformation and rotational inertia in their studies (Davis et al. 1972a, b). Yamada and Ezawa took a differential equations approach and presented the stiffness matrix of a finite curved element under three internal loads in 1977 (Yamada and Ezawa 1977). In 1981, Yoo and Fehrenbach presented a finite curved element for the free vibration of a horizontal, curved beam that ignored the effects of shear deformation (Yoo and Fehrenbach 1981). Palaninathan and Chandrasekharan used the Castigliano's theorem and obtained the stiffness matrix of a curved Timoshenko beam in three dimensions. They also accounted for the effects of coupling of vertical and lateral shear loads (Palaninathan and Chandrasekharan 1985).

In their 2006 study, Yoon et al. drew on the approach taken by Yang and Kuo and investigated the out-of-plane dynamic behavior of thin-walled curved beams. They considered the effects of warping and obtained the equations governing thin-walled curved beams with seven degrees of freedom in each node (Yang and Kuo 1996; Yoon et al. 2006). In 2015, Horibe and Mori investigated the in-plane and out-of-plane deflection of a J-shaped beam, which was clamped at one end and was free at the other, subjected to a point load. They obtained an analytical solution by numerically combining the modified elliptical integral and differentiating the beam's strain energy using Castigliano's theorem. The study showed that the beam stresses and deflection could be calculated by applying in-plane and out-of-plane loads simultaneously (Horibe and Mori 2015). In 2018, Marotta and Salvini proposed a closed solution for the stiffness matrix of a curved beam using Castigliano's second theorem and considering bending and axial effects. This analytical solution was obtained using a curved beam by a third-degree function for the curvature radius. They concluded that this method is also suitable for nonlinear analysis with considerable displacement (Marotta and Salvini 2018).

The present study introduces quasi-X braces and calculates the elastic stiffness of steel moment frames equipped with these braces accurately. Adding these braces to the moment frame improves the system's stiffness and prevents excessive structural deformation. Here, an accurate, practical formulation was first presented by a novel method for calculating the elastic stiffness of two-dimensional single-span and one-story steel moment frames equipped with quasi-X braces under lateral loading. Where all effective parameters, including the axial loads, shear loads, and bending moments of all members, were taken into account. The relation was then evaluated for different cases using the finite element software, OpenSees. Showing little error, the results of the proposed relation are consistent with the numerical finite element analysis (FEA). Then, the seismic performance of QXB-MF systems was examined as per the FEMA P695 methodology for near-field and far-field ground motion records compared with the intermediate moment frame. The outcomes revealed that employing quasi-X braces in the intermediate moment frame improves the seismic performance of this system.

2 A new method for calculating the elastic stiffness of the quasi-X-braced steel moment frames

In this part of the study, the lateral stiffness of the two-dimensional single-span and one-story quasi-X-braced steel moment frame (QXB-MF) and quasi inverse-X-braced steel moment frame (QIXB-MF) comprising four connected quarter-elliptic bracing components under a lateral load of P (Fig. 3) is determined by a new method and based on the concept of strain

energy and Castigliano's theorem (Hibbeler and Kiang 2015), considering axial, shear, and bending deformations.

Due to the geometric characteristics of these two bracing systems, the final analytical formulation for the elastic stiffness of both bracing systems is the same; therefore, in this section, only the calculation steps for the QXB-MF system are presented. The braced frame was treated as a half-frame (Fig. 4a) where the length of the half-beam $(L_b/2)$ is equal to the semi-major-axis of the ellipse (a) and the length of the half-column $(L_c/2)$ is equal to the semi-minor-axis of the ellipse (b) to allow for using structural analysis relations for symmetric structures under asymmetric loading and simplify calculations. Moreover, the specifications of the beam, column, and bracing components were considered with a parametric representation. Equation (1) expresses the geometric specifications of the frame (Fig. 4a).

$$\tan\theta = \frac{b}{a} = \frac{L_c}{L_b} = e, \sin\theta = \frac{b}{\sqrt{a^2 + b^2}} = \frac{e}{\sqrt{1 + e^2}}, \cos\theta = \frac{a}{\sqrt{a^2 + b^2}} = \frac{1}{\sqrt{1 + e^2}} \quad (1)$$

where θ denotes the orientation angle of the quarter-elliptic component in the half-frame. According to Fig. 4a and using equations of compatibility for the braced half-frame, the vertical load in node E is:

$$\sum F_y = 0 \rightarrow R_C + R_D + R_E = \frac{PL_c}{L_b} \rightarrow R_E = \frac{PL_c}{L_b} - R_C - R_D \quad (2)$$

Figure 4b shows the internal efforts of the braced half-frame under a lateral load of $P/2$ considering F_{AD} and F_{DA} on the two sides of the braced quarter-elliptic section AD and F_{BD} and F_{DB} on the two sides of the braced quarter-elliptic section BD.

The internal efforts of the half-frame members were calculated for nodes $A, B, C, D,$ and E based on equations of compatibility and according to Fig. 5. For node A (Fig. 5a):

$$M_{AE} = M_{AB} \quad (3)$$

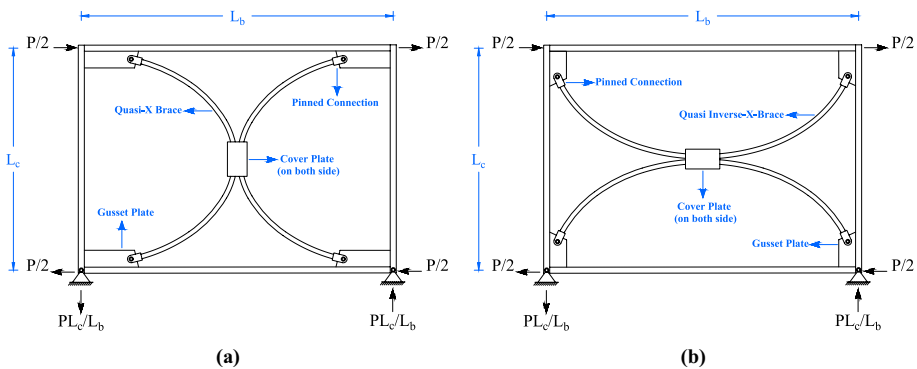$$\sum F_x = 0 \rightarrow N_{AE} + F_{AD}\cos\theta - V_{AB} = \frac{P}{2} \quad (4)$$

Fig. 3 Desired steel moment frames with directly welded rigid connections equipped with quasi-X brace; **a** QXB-MF, **b** QIXB-MF
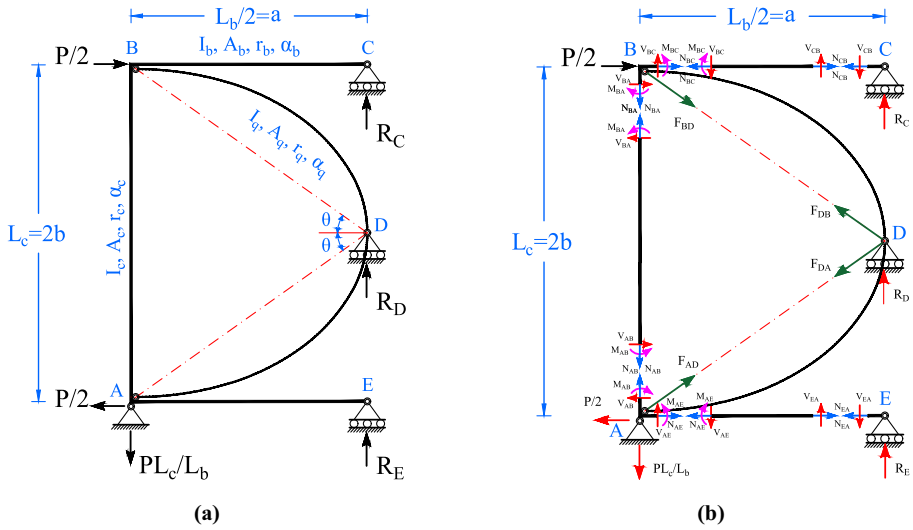
Fig. 4 Quasi-X-braced steel moment frame (QXB-MF); **a** braced half-frame after splitting the steel moment frame, **b** Internal efforts of the half-braced frame

$$\sum F_y = 0 \rightarrow N_{AB} + F_{AD}\sin\theta + V_{AE} = \frac{PL_c}{L_b} \tag{5}$$
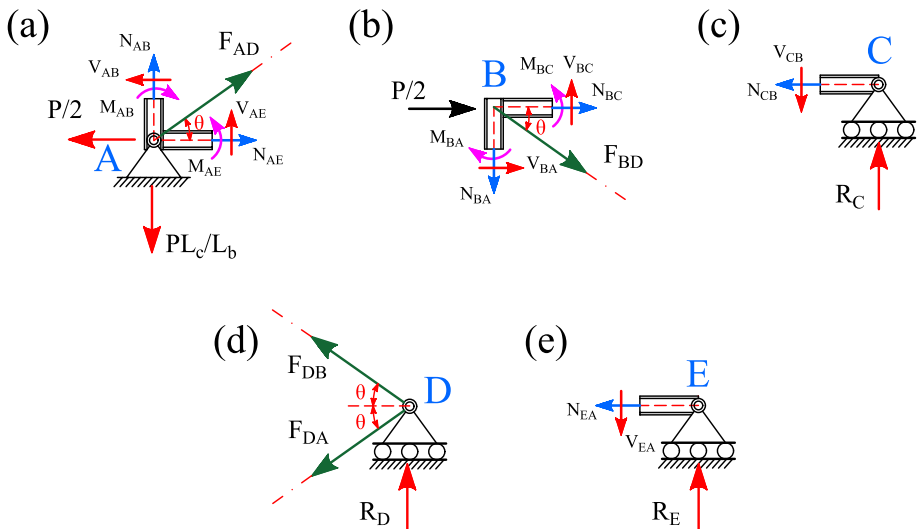
For node B (Fig. 5b):

$$M_{BA} = M_{BC} \tag{6}$$

Fig. 5 Analysis of joints in the half-braced frame; **a** joint A, **b** joint B, **c** joint C, **d** joint D, **e** joint E

$$\sum F_x = 0 \rightarrow \frac{P}{2} + F_{BD}\cos\theta + N_{BC} + V_{BA} = 0 \rightarrow N_{BC} = -V_{BA} - \frac{P}{2} - F_{BD}\cos\theta \quad (7)$$

$$\sum F_y = 0 \rightarrow N_{BA} + F_{BD}\sin\theta - V_{BC} = 0- \rightarrow N_{BA} = V_{BC} - F_{BD}\sin\theta \quad (8)$$

For node C (Fig. 5c):

$$\sum F_x = 0 \rightarrow N_{CB} = 0 \quad (9)$$

$$\sum F_y = 0 \rightarrow R_C = V_{CB} \quad (10)$$

For node D (Fig. 5d):

$$\sum F_x = 0 \rightarrow F_{DB}\cos\theta + F_{DA}\cos\theta = 0 \rightarrow F_{DA} = -F_{DB} \quad (11)$$

$$\sum F_y = 0 \rightarrow F_{DB}\sin\theta - F_{DA}\sin\theta + R_D = 0 \rightarrow R_D = F_{DA}\sin\theta - F_{DB}\sin\theta \quad (12)$$

For node E (Fig. 5e):

$$\sum F_x = 0 \rightarrow N_{EA} = 0 \quad (13)$$

$$\sum F_y = 0 \rightarrow R_E = V_{EA} \quad (14)$$

Figure 6 shows the internal efforts of beams AE and BC and column AB. The shear and axial loads on the two sides of the members were calculated based on equations of static equilibrium and the moment at two endpoints of the beams and column. For beam BC (Fig. 6a):

$$N_{BC} = N_{CB} \quad (15)$$

$$V_{BC} = V_{CB} \quad (16)$$

$$\sum M_C = 0 \rightarrow M_{BC} - V_{BC} \times \frac{L_b}{2} = 0 \rightarrow V_{BC} = \frac{2M_{BC}}{L_b} \quad (17)$$

For beam AE (Fig. 6b):

$$N_{AE} = N_{EA} \quad (18)$$

$$V_{AE} = V_{EA} \quad (19)$$

$$\sum M_E = 0 \rightarrow M_{AE} - V_{AE} \times \frac{L_b}{2} = 0 \rightarrow V_{AE} = \frac{2M_{AE}}{L_b} \quad (20)$$
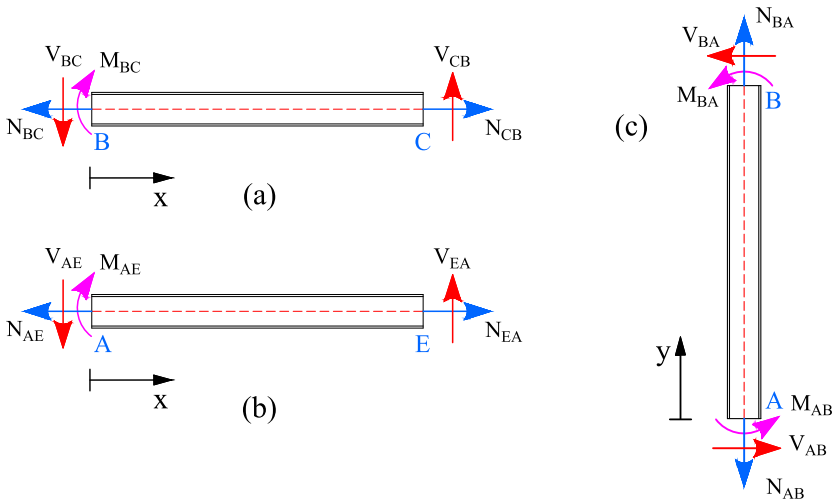
For column AB (Fig. 4c):

Fig. 6 Internal efforts; **a** beam BC, **b** beam AE, **c** column AB

$$N_{AB} = N_{BA} \tag{21}$$

$$V_{AB} = V_{BA} \tag{22}$$

The vertical load at E was calculated by substituting Eqs. (10), (16), and (17) in the second phrase and Eqs. (11) and (12) in the third phrase of Eq. (2):

$$R_E = \frac{PL_c}{L_b} - \frac{2M_{BC}}{L_b} - 2F_{DA} \sin\theta \tag{23}$$

The internal efforts of the quarter-elliptic bracing member AD were calculated by substituting Eqs. (14), (19), and (20) in Eq. (23) as follows:

$$\frac{2M_{AE}}{L_b} = \frac{PL_c}{L_b} - \frac{2M_{BC}}{L_b} - 2F_{DA}\sin\theta \rightarrow F_{DA} = F_{AD} = \frac{PL_c}{2L_b \sin\theta} - \frac{M_{BC}}{L_b \sin\theta} - \frac{M_{AE}}{L_b \sin\theta}a \tag{24}$$

The internal efforts of the quarter-elliptic bracing member BD were calculated by substituting Eq. (24) in Eq. (11) as follows:

$$F_{DB} = F_{BD} = -\frac{PL_c}{2L_b \sin\theta} + \frac{M_{BC}}{L_b \sin\theta} + \frac{M_{AE}}{L_b \sin\theta} \tag{25}$$

Substituting Eqs. (13), (18), and (24) in Eq. (4) produced a new relation that was simplified using Eq. (1) to obtain shear in the AB column as follows:

$$\left(\frac{PL_c}{2L_b \sin\theta} - \frac{M_{BC}}{L_b \sin\theta} - \frac{M_{AE}}{L_b \sin\theta} \right) \cos\theta = V_{AB} + \frac{P}{2} \rightarrow V_{AB}$$

$$= \frac{PL_c}{2L_b \tan\theta} - \frac{M_{BC}}{L_b \tan\theta} - \frac{M_{AE}}{L_b \tan\theta} - \frac{P}{2} \quad (26)$$

$$= -\frac{M_{BC}}{eL_b} - \frac{M_{AE}}{eL_b}$$

Steel's shear modulus (G) was obtained based on Young's modulus (E) and Poisson's ratio (ν) in Eq. (27):

$$G = \frac{E}{2(1+\nu)}, \nu = 0.3 \rightarrow G = \frac{E}{2(1+0.3)} = \frac{E}{2.6} \quad (27)$$

The total and effective shear area of the column cross-section (Fig. 4a) are expressed by Eq. (28), those of the beam cross-section by Eq. (29), and those of the bracing cross-section by Eq. (30):

$$A'_c = \frac{A_c}{\alpha_c}, \quad A_c = \frac{I_c}{r_c^2} \quad (28)$$

$$A'_b = \frac{A_b}{\alpha_b}, \quad A_b = \frac{I_b}{r_b^2} \quad (29)$$

$$A'_q = \frac{A_q}{\alpha_q}, \quad A_q = \frac{I_q}{r_q^2} \quad (30)$$

where in these equations, A signifies the cross-sectional area, A' the effective shear area of the cross-section, α the shear shape coefficient of the cross-section, and I and r denote the moment of inertia and the radius of gyration of the cross-section around the bending axis (strong axis), respectively.

2.1 Calculating strain energy of the column

The strain energy was calculated based on the internal bending moment, internal axial load, and the internal shear load for the column. The strain energy of the column was calculated by obtaining the changes of the internal forces in the column AB according to Fig. 6b and then obtaining the strain energy stored in the column based on the general energy equation. Equation (31) shows the column's internal moment:

$$M_{AB}(y) = M_{AB} + V_{AB}y, \quad 0 \le y \le L_c \quad (31)$$

The strain energy resulting from bending, axial, and shear deformation of the column is calculated from Eq. (32). where E represents Young's modulus and G is the steel's shear modulus as obtained in Eq. (27). A_c denotes the column's cross-sectional area, and A'_c is its effective shear cross-section as obtained in Eq. (28).

$$
\begin{aligned}
U_{AB} &= \frac{1}{2EI_c} \int_0^{L_c} M_{AB}^2(y)dy + \frac{V_{AB}^2 L_c}{2GA_c'} + \frac{N_{AB}^2 L_c}{2EA_c} \\
&= \frac{1}{2EI_c} \int_0^{L_c} \left(M_{AB} + V_{AB}y\right)^2 dy + 2.6\alpha_c \frac{V_{AB}^2 L_c}{2EA_c} + \frac{N_{AB}^2 L_c}{2EA_c} \\
&= \frac{1}{2EI_c} \int_0^{L_c} \left(M_{AB}^2 + 2M_{AB}V_{AB}y + V_{AB}^2 y^2\right)dy + \frac{\left(2.6\alpha_c V_{AB}^2 + N_{AB}^2\right)L_c}{2EA_c} \\
&= \frac{M_{AB}^2 L_c}{2EI_c} + \frac{M_{AB}V_{AB}L_c^2}{2EI_c} + \frac{V_{AB}^2 L_c^3}{6EI_c} + \frac{\left(2.6\alpha_c V_{AB}^2 + N_{AB}^2\right)L_c r_c^2}{2EI_c}
\end{aligned}
\tag{32}
$$

N_{AB} was obtained by substituting Eqs. (17), (21), and (25) in Eq. (8), and substituting of this equation, Eqs. (1), (22), and (26) in Eq. (32) produces the strain energy of the *AB* column:

$$
\begin{aligned}
U_{column,\,bav} = U_{AB} &= \frac{M_{AE}^2 L_c}{2EI_c} + \frac{M_{AE}\left(-\frac{M_{BC}}{eL_b} - \frac{M_{AE}}{eL_b}\right)L_c^2}{2EI_c} \\
&+ \frac{\left(-\frac{M_{BC}}{eL_b} - \frac{M_{AE}}{eL_b}\right)^2 L_c^3}{6EI_c} + \frac{\left(2.6\alpha_c V_{AB}^2 + N_{AB}^2\right)L_c r_c^2}{2EI_c} \\
&= \frac{L_c}{6EI_c}\left[3M_{AE}^2 + 3M_{AE}(-M_{BC} - M_{AE}) + (-M_{BC} - M_{AE})^2\right] \\
&+ 3r_c^2\left(2.6\alpha_c\left(-\frac{M_{BC}}{eL_b} - \frac{M_{AE}}{eL_b}\right)^2 + \left(\frac{2M_{BC} - 2M_{AE} + PL_c}{2L_b}\right)^2\right)\Big] \\
&= \frac{L_c}{6EI_c}\left[M_{BC}^2 - M_{BC}M_{AE} + M_{AE}^2 + \frac{7.8\alpha_c r_c^2}{L_c^2}\left(M_{BC}^2 + 2M_{BC}M_{AE} + M_{AE}^2\right)\right] \\
&+ \frac{3r_c^2}{4L_b^2}\left(4M_{BC}^2 + 4M_{AE}^2 + P^2 L_c^2 - 8M_{BC}M_{AE} + 4M_{BC}PL_c - 4M_{AE}PL_c\right)\Big]
\end{aligned}
\tag{33}
$$

2.2 Calculating strain energy of the beams

The strain energy was calculated based on the internal bending moment, internal axial load, and internal shear load for the beams. The strain energy of the beams was calculated by obtaining the changes of the internal forces in the beams *AE* and *BC* according to Fig. 6a and then obtaining the strain energy stored in the beams based on the general energy equation. The values of the internal moment of the beams are acquired in Eqs. (34) and (35):

$$
M_{AE}(x) = M_{AE} - V_{AE}x, \quad 0 \le x \le \frac{L_b}{2}
\tag{34}
$$

$$
M_{BC}(x) = M_{BC} - V_{BC}x, \quad 0 \le x \le \frac{L_b}{2}
\tag{35}
$$

The strain energy resulting from bending, axial, and shear deformation of the beams is calculated from Eqs. (36) and (37). where *E* represents Young's modulus and *G* is the

steel's shear modulus as obtained in Eq. (27). A_b denotes the beam's cross-sectional area, and A'_b is its effective shear cross-section as obtained in Eq. (29).

$$
\begin{aligned}
U_{AE} &= \frac{1}{2EI_b} \int_0^{\frac{L_b}{2}} M_{AE}^2(x)dx + \frac{V_{AE}^2\left(\frac{L_b}{2}\right)}{2GA'_b} + \frac{N_{AE}^2\left(\frac{L_b}{2}\right)}{2EA_b} \\
&= \frac{1}{2EI_b} \int_0^{\frac{L_b}{2}} \left(M_{AE} - V_{AE}x\right)^2 dx + 2.6\alpha_b\frac{V_{AE}^2 L_b}{4EA_b} + \frac{N_{AE}^2 L_b}{4EA_b} \\
&= \frac{1}{2EI_b} \int_0^{\frac{L_b}{2}} \left(M_{AE}^2 - 2M_{AE}V_{AE}x + V_{AE}^2 x^2\right)dx + \frac{\left(2.6\alpha_b V_{AE}^2 + N_{AE}^2\right)L_b}{4EA_b} \\
&= \frac{M_{AE}^2 L_b}{4EI_b} - \frac{M_{AE}V_{AE}L_b^2}{8EI_b} + \frac{V_{AE}^2 L_b^3}{48EI_b} + \frac{\left(2.6\alpha_b V_{AE}^2 + N_{AE}^2\right)L_b r_b^2}{4EI_b}
\end{aligned}
\tag{36}
$$

$$
\begin{aligned}
U_{BC} &= \frac{1}{2EI_b} \int_0^{\frac{L_b}{2}} M_{BC}^2(x)dx + \frac{V_{BC}^2\left(\frac{L_b}{2}\right)}{2GA'_b} + \frac{N_{BC}^2\left(\frac{L_b}{2}\right)}{2EA_b} \\
&= \frac{1}{2EI_b} \int_0^{\frac{L_b}{2}} \left(M_{BC} - V_{BC}x\right)^2 dx + 2.6\alpha_b\frac{V_{BC}^2 L_b}{4EA_b} + \frac{N_{BC}^2 L_b}{4EA_b} \\
&= \frac{1}{2EI_b} \int_0^{\frac{L_b}{2}} \left(M_{BC}^2 - 2M_{BC}V_{BC}x + V_{BC}^2 x^2\right)dx + \frac{\left(2.6\alpha_b V_{BC}^2 + N_{BC}^2\right)L_b}{4EA_b} \\
&= \frac{M_{BC}^2 L_b}{4EI_b} - \frac{M_{BC}V_{BC}L_b^2}{8EI_b} + \frac{V_{BC}^2 L_b^3}{48EI_b} + \frac{\left(2.6\alpha_b V_{BC}^2 + N_{BC}^2\right)L_b r_b^2}{4EI_b}
\end{aligned}
\tag{37}
$$

According to Eqs. (13) and (18), N_{AE} is 0, and substituting Eqs. (19) and (20) in Eq. (36) yields the strain energy of the beam AE:

$$
\begin{aligned}
U_{AE} &= \frac{M_{AE}^2 L_b}{4EI_b} - \frac{M_{AE}\left(\frac{2M_{AE}}{L_b}\right)L_b^2}{8EI_b} + \frac{\left(\frac{2M_{AE}}{L_b}\right)^2 L_b^3}{48EI_b} + \frac{\left(2.6\alpha_b V_{AE}^2\right)L_b r_b^2}{4EI_b} \\
&= \frac{L_b}{12EI_b}\left[M_{AE}^2 + 3r_b^2\left(2.6\alpha_b\left(\frac{2M_{AE}}{L_b}\right)^2\right)\right] \\
&= \frac{L_b}{12EI_b}\left[M_{AE}^2 + \frac{31.2\alpha_b r_b^2}{L_b^2}\left(M_{AE}^2\right)\right]
\end{aligned}
\tag{38}
$$

According to Eqs. (9) and (15), N_{BC} is 0, and substituting Eqs. (16) and (17) in Eq. (37) yields the strain energy of the beam BC:

$$U_{BC} = \frac{M_{BC}^2 L_b}{4EI_b} - \frac{M_{BC}\left(\frac{2M_{BC}}{L_b}\right)L_b^2}{8EI_b} + \frac{\left(\frac{2M_{BC}}{L_b}\right)^2 L_b^3}{48EI_b} + \frac{(2.6\alpha_b V_{BC}^2)L_b r_b^2}{4EI_b}$$

$$= \frac{L_b}{12EI_b}\left[M_{BC}^2 + 3r_b^2\left(2.6\alpha_b\left(\frac{2M_{BC}}{L_b}\right)^2\right)\right] \tag{39}$$

$$= \frac{L_b}{12EI_b}\left[M_{BC}^2 + \frac{31.2\alpha_b r_b^2}{L_b^2}\left(M_{BC}^2\right)\right]$$

The total strain energy resulting from bending, axial, and shear deformation of beams was obtained by summing up Eqs. (38) and (39):

$$U_{beams,bav} = U_{AE} + U_{BC} = \frac{L_b}{12EI_b}\left[M_{AE}^2 + M_{BC}^2 + \frac{31.2 r_b^2}{L_b^2}\left(M_{AE}^2 + M_{BC}^2\right)\right] \tag{40}$$

2.3 Calculating strain energy of the quarter-elliptic bracing member

The strain energy was calculated based on the internal bending moment, internal axial load, and internal shear load for the quarter-elliptic bracing member. The strain energy of the quarter-elliptic bracing member was calculated by obtaining the changes of the internal forces in the brace *BD* according to Fig. 7, and the elliptic equation (Eq. (41)). Then, the strain energy stored in the bracing member is obtained based on the general energy equation.

$$\frac{x^2}{a^2} + \frac{y^2}{b^2} = 1 \rightarrow y = b\sqrt{1 - \frac{x^2}{a^2}}, \quad 0 \le x \le a \tag{41}$$

An infinitesimal arc length (*ds*) was considered for an arbitrary point in (x, y) coordinates using Eq. (42).

$$ds = \sqrt{dx^2 + dy^2} = \sqrt{1 + \left(\frac{dy}{dx}\right)^2}\,dx = \sqrt{1 + y'^2}\,dx \tag{42}$$

The inclination angle of the tangent line from any point relative to the horizontal axis (ϕ) was obtained for the quarter-elliptic bracing component using Eq. (41).

$$y' = -b.\frac{\frac{x}{a^2}}{\sqrt{1 - \frac{x^2}{a^2}}} \rightarrow |y'| = tan\phi \tag{43}$$

Based on Eq. (43) and making use of trigonometric identities (Pythagorean identities), $sin\phi$ and $cos\phi$ were obtained in terms of x in Eqs. (44) and (45):

$$1 + tan^2\phi = \frac{1}{cos^2\phi} \rightarrow cos^2\phi = \frac{1}{1 + tan^2\phi} = \frac{1}{1 + \frac{b^2 \frac{x^2}{a^4}}{1 - \frac{x^2}{a^2}}} = \frac{1}{\frac{1 - \frac{x^2}{a^2} + \frac{b^2 x^2}{a^4}}{1 - \frac{x^2}{a^2}}}$$

$$= \frac{1 - \frac{x^2}{a^2}}{1 - \frac{x^2}{a^2} + \frac{b^2 x^2}{a^4}} \rightarrow cos\phi = \sqrt{\frac{1 - \frac{x^2}{a^2}}{1 - \frac{x^2}{a^2} + \frac{b^2 x^2}{a^4}}} \tag{44}$$

$$sin^2\phi = 1 - cos^2\phi = \frac{1 - \frac{x^2}{a^2} + \frac{b^2 x^2}{a^4} - 1 + \frac{x^2}{a^2}}{1 - \frac{x^2}{a^2} + \frac{b^2 x^2}{a^4}}$$

$$= \frac{\frac{b^2 x^2}{a^4}}{1 - \frac{x^2}{a^2} + \frac{b^2 x^2}{a^4}} \rightarrow sin\phi = \frac{b \frac{x}{a^2}}{\sqrt{1 - \frac{x^2}{a^2} + \frac{b^2 x^2}{a^4}}} \tag{45}$$

Static equilibrium was used to find the internal bending, axial, and shear efforts of the quarter-elliptic bracing member according to Fig. 7:

$$F_{BD} = F_{DB} = F \tag{46}$$

$$\sum F_x = 0 \rightarrow Fcos\theta = N(x)cos\phi + V(x)sin\phi \tag{47}$$

$$\sum F_y = 0 \rightarrow Fsin\theta = N(x)sin\phi - V(x)cos\phi \tag{48}$$

$$\sum M_G = 0 \rightarrow M(x) = Fsin\theta.x - Fb\left(1 - \sqrt{1 - \frac{x^2}{a^2}}\right)cos\theta \tag{49}$$

$sin\theta$ and $cos\theta$ depend on the lengths of the beam $(L_b/2)$ and column $(L_c/2)$. Solving the system of Eqs. (47) and (48) the axial and shear loads of the quarter-elliptic bracing member was obtained in terms of x:

$$N(x) = F(cos\theta cos\phi + sin\theta sin\phi) \tag{50}$$

Fig. 7 Internal efforts of the element *BD* in the quasi-X brace
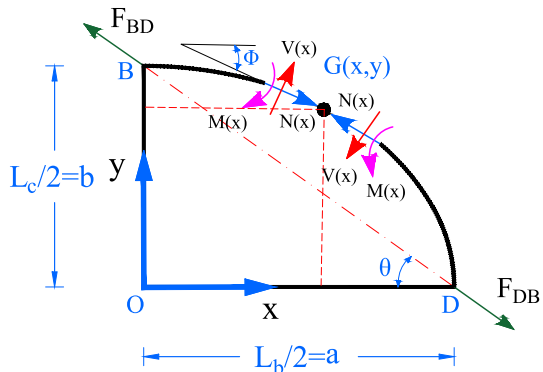
$$V(x) = F(cos\theta sin\phi - sin\theta cos\phi) \tag{51}$$

Based on the general energy equation and Eq. (42), the strain energy stored in the quarter-elliptic bracing member under internal bending moment, the internal axial load, and internal shear are as follows:

$$
\begin{aligned}
U_{quarter-elliptic\ brace,\ bav} &= U_b + U_a + U_v = \int \frac{M(x)^2}{2EI_q}ds + \int \frac{N(x)^2}{2EA_q}ds + \int \frac{V(x)^2}{2GA'_q}ds \\
&= \int_0^a \frac{M(x)^2}{2EI_q}.\sqrt{1+y'^2}dx + \int_0^a \frac{N(x)^2}{2EA_q}.\sqrt{1+y'^2}dx + \int_0^a \frac{V(x)^2}{2GA'_q}.\sqrt{1+y'^2}dx
\end{aligned}
\tag{52}
$$

where

$$
\sqrt{1+y'^2} = \sqrt{1 + \frac{b^2\frac{x^2}{a^4}}{1-\frac{x^2}{a^2}}} = \sqrt{\frac{1 - \frac{x^2}{a^2} + b^2\frac{x^2}{a^4}}{1 - \frac{x^2}{a^2}}}
\tag{53}
$$

where E represents Young's modulus, and G is the steel's shear modulus obtained in Eq. (27). A_q denotes the quarter-elliptic bracing member's cross-sectional area, and A'_q is its effective shear cross-section as obtained in Eq. (30). The strain energy of the quarter-elliptic member under internal bending moment was obtained by substituting Eqs. (1), (49), and (53) in the first phrase of Eq. (52):

$$
\begin{aligned}
U_b &= \frac{F^2}{2EI_q} \int_0^a \left[sin\theta.x - bcos\theta.\left(1 - \sqrt{1-\frac{x^2}{a^2}}\right)\right]^2 \times \frac{\sqrt{1 - \frac{x^2}{a^2} + b^2\frac{x^2}{a^4}}}{\sqrt{1-\frac{x^2}{a^2}}}dx \\
&= \frac{F^2b^2}{2EI_q.(1+e^2)} \int_0^a \left[\frac{x}{a} - \left(1 - \sqrt{1-\frac{x^2}{a^2}}\right)\right]^2 \times \frac{\sqrt{1 - \frac{x^2}{a^2} + e^2\frac{x^2}{a^2}}}{\sqrt{1-\frac{x^2}{a^2}}}dx
\end{aligned}
\tag{54}
$$

The integral in Eq. (54) was solved by a change of variables based on Eq. (55):

$$t = \frac{x}{a} \rightarrow dt = \frac{dx}{a} \rightarrow dx = a.dt \tag{55}$$

By substituting Eq. (55) in Eq. (54), we have:

$$U_b = \frac{F^2ab^2}{2EI_q} \int_0^1 \frac{\left[t - 1 + \sqrt{1-t^2}\right]^2.\sqrt{1 + (e^2 - 1).t^2}}{(1+e^2).\sqrt{1-t^2}}dt \tag{56}$$

If:

$$\lambda_b(e) = \int_0^1 \frac{\left[t - 1 + \sqrt{1-t^2}\right]^2.\sqrt{1 + (e^2 - 1).t^2}}{(1+e^2).\sqrt{1-t^2}}dt \tag{57}$$

Then, strain energy under internal bending moment in the quarter-elliptic bracing member is:

$$U_b = \frac{F^2 ab^2}{2EI_q} . \lambda_b(e) \qquad (58)$$

$\lambda_b(e)$ is a function of e (ratio of the half of the column's length to half of the beam's length) that can be solved numerically. Figure 8 plots $\lambda_b(e)$ in a diagram for different e values. The strain energy of the quarter-elliptic member under internal bending moment was obtained by substituting Eqs. (1), (50), and (53) in the second phrase of Eq. (52):

$$
\begin{aligned}
U_a &= \frac{F^2}{2EA_q} \int_0^a [cos\theta cos\phi + sin\theta sin\phi]^2 \times \frac{\sqrt{1 - \frac{x^2}{a^2} + e^2 \frac{x^2}{a^2}}}{\sqrt{1 - \frac{x^2}{a^2}}} dx \\
&= \frac{F^2}{2EA_q} \int_0^a \left[\frac{1}{\sqrt{1+e^2}} . \frac{\sqrt{1 - \frac{x^2}{a^2}}}{\sqrt{1 - \frac{x^2}{a^2} + e^2 \frac{x^2}{a^2}}} + \frac{e}{\sqrt{1+e^2}} . \frac{e\frac{x}{a}}{\sqrt{1 - \frac{x^2}{a^2} + e^2 \frac{x^2}{a^2}}} \right]^2 \\
&\quad \times \frac{\sqrt{1 - \frac{x^2}{a^2} + e^2 \frac{x^2}{a^2}}}{\sqrt{1 - \frac{x^2}{a^2}}} dx
\end{aligned}
\qquad (59)
$$

The integral in Eq. (59) was solved by a change of variables based on Eq. (55). By substituting Eq. (55) in Eq. (59), we have:

$$U_a = \frac{F^2 a}{2EA_q} . \int_0^1 \frac{1}{(1+e^2)} . \frac{\left[\sqrt{1-t^2} + e^2 t\right]^2}{\sqrt{(1-t^2).[1 + (e^2-1)t^2]}} dt \qquad (60)$$

If:

$$\lambda_a(e) = \int_0^1 \frac{1}{(1+e^2)} . \frac{\left[\sqrt{1-t^2} + e^2 t\right]^2}{\sqrt{(1-t^2).[1 + (e^2-1)t^2]}} dt \qquad (61)$$

Then, strain energy under internal axial force in the quarter-elliptic bracing member is:

$$U_a = \frac{F^2 a}{2EA_h} . \lambda_a(e) \qquad (62)$$

$\lambda_a(e)$ is a function of e (ratio of the half of the column's length to half of the beam's length) that can be solved numerically. Figure 8 plots $\lambda_a(e)$ in a diagram for different e values. The strain energy of the quarter-elliptic member under internal shear force was obtained by substituting Eqs. (1), (51), and (53) in the third phrase of Eq. (52):
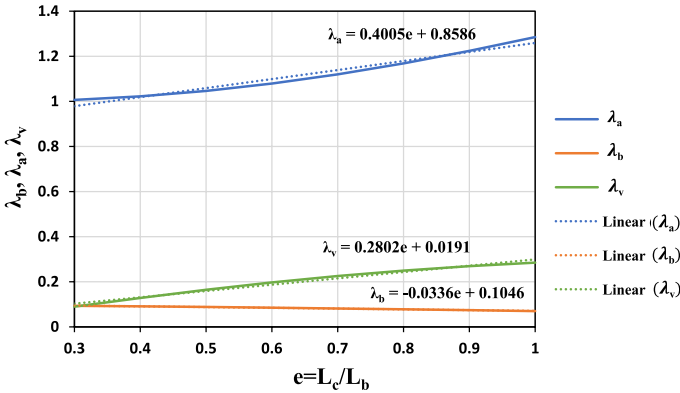
Fig. 8 The $\lambda_b(e)$, $\lambda_a(e)$, and $\lambda_v(e)$ parameters as a function of parameter e

$$U_v = \frac{\alpha_q \cdot F^2}{2GA_q} \int_0^a [cos\theta sin\phi - sin\theta cos\phi]^2 \times \frac{\sqrt{1 - \frac{x^2}{a^2} + e^2\frac{x^2}{a^2}}}{\sqrt{1 - \frac{x^2}{a^2}}} dx$$

$$= \alpha_q \cdot \frac{F^2}{2GA_q} \int_0^a \left[\frac{1}{\sqrt{1+e^2}} \cdot \frac{e \cdot \frac{x}{a}}{\sqrt{1 - \frac{x^2}{a^2} + e^2\frac{x^2}{a^2}}} - \frac{e}{\sqrt{1+e^2}} \cdot \frac{\sqrt{1 - \frac{x^2}{a^2}}}{\sqrt{1 - \frac{x^2}{a^2} + e^2\frac{x^2}{a^2}}} \right]^2 \quad (63)$$

$$\times \frac{\sqrt{1 - \frac{x^2}{a^2} + e^2\frac{x^2}{a^2}}}{\sqrt{1 - \frac{x^2}{a^2}}} dx$$

The integral in Eq. (63) was solved by a change of variables based on Eq. (55). By substituting Eq. (55) in Eq. (63), we have:

$$U_v = \alpha_q \cdot \frac{F^2 a}{2GA_q} \cdot \int_0^1 \frac{e^2}{(1+e^2)} \cdot \frac{\left[t - \sqrt{1-t^2}\right]^2}{\sqrt{(1-t^2) \cdot [1 + (e^2-1)t^2]}} dt \quad (64)$$

If:

$$\lambda_v(e) = \int_0^1 \frac{e^2}{(1+e^2)} \cdot \frac{\left[t - \sqrt{1-t^2}\right]^2}{\sqrt{(1-t^2) \cdot [1 + (e^2-1)t^2]}} dt \quad (65)$$

Then, strain energy under internal shear force in the quarter-elliptic bracing member is:

$$U_v = \alpha_q \cdot \frac{F^2.a}{2GA_q} \cdot \lambda_v(e) \tag{66}$$

$\lambda_v(e)$ is a function of e (ratio of the half of the column's length to half of the beam's length) that can be solved numerically. Figure 8 plots $\lambda_v(e)$ in a diagram for different e values.

By substituting Eqs. (58), (62), and (66) in Eq. (52), the strain energy stored in the quarter-elliptic bracing member *BD* was simplified as follows:

$$
\begin{aligned}
U_{BD} = U_b + U_a + U_v &= \frac{F^2ab^2}{2EI_q} \cdot \lambda_b(e) + \frac{F^2a}{2EA_q} \cdot \lambda_a(e) + \alpha_q \cdot \frac{F^2 \cdot a}{2GA_q} \cdot \lambda_v(e) \\
&= \frac{F^2.a}{2EA_q}\left[\left(\frac{b}{r_q} \right)^2 \cdot \lambda_b + \lambda_a + 2.6\alpha_q\lambda_v \right] = \frac{F^2.a}{2EA_q} \cdot \frac{\lambda_{bav}}{1+e^2}
\end{aligned}
\tag{67}
$$

where:

$$\lambda_{bav} = \left[\left(\frac{b}{r_q} \right)^2 \cdot \lambda_b + \lambda_a + 2.6\alpha_q\lambda_v \right] \cdot \left(1 + e^2 \right) \tag{68}$$

$\lambda_{bav}(e)$ is a function of e (ratio of the half of the column's length to half of the beam's length) that can be solved numerically. $\lambda_{bav}(e)$ was plotted for different e values in Fig. 9, considering a shear shape coefficient of 2 for the quarter-elliptic bracing cross-section (BOX sections). By fitting λ_b, λ_a, and λ_v curves with linear regression in Fig. 8 and substituting the resulting linear equations in Eq. (68), $\lambda_{bav}(e)$ was found:

$$\lambda_{bav} = \left[\left(\frac{b}{r_q} \right)^2 .(-0.0336e + 0.1046) + (0.4005e + 0.8586) + 2.6\alpha_q.(0.2802e + 0.0191) \right].\left(1 + e^2\right) \tag{69}$$

Substituting Eqs. (1) and (25) in Eq. (67) helped calculate the stored strain energy of the bracing member *BD*:

$$U_{BD} = \frac{a.\lambda_{bav}}{2EA_qL_c^2}\left(-\frac{PL_c}{2} + M_{BC} + M_{AE} \right)^2 \tag{70}$$

Substituting Eqs. (1) and (24) in Eq. (67) helped calculate the stored strain energy of the bracing member *AD*:

$$U_{AD} = \frac{a.\lambda_{bav}}{2EA_qL_c^2}\left(\frac{PL_c}{2} - M_{BC} - M_{AE} \right)^2 \tag{71}$$

The strain energy resulting from bending, axial, and shear deformation was obtained for the half-elliptic member by summing up Eqs. (70) and (71):

$$U_{half-elliptic\ brace,bav} = U_{BD} + U_{AD} = \frac{a.\lambda_{bav}}{EA_qL_c^2} \times \left(-\frac{PL_c}{2} + M_{AE} + M_{BC} \right)^2 \tag{72}$$

2.4 Strain energy of the quasi-X-braced steel moment frames (QXB-MFs)

The strain energy of the braced half-frame was obtained by summing up the strain energy (resulting from bending, axial, and shear deformation) of the columns, beams, and the half-elliptic bracing member according to Eqs. (33), (40), and (72):

$$
\begin{aligned}
U &= U_{column,bav} + U_{beams,bav} + U_{half-elliptic\ brace,bav} \\
&= R.\left(\begin{array}{c} M_{BC}^2 - M_{BC}M_{AE} + M_{AE}^2 + \kappa_c.\left(M_{BC}^2 + 2M_{BC}M_{AE} + M_{AE}^2\right) \\ +\mu_c.\left(4M_{BC}^2 + 4M_{AE}^2 + P^2L_c^2 - 8M_{BC}M_{AE} + 4M_{BC}PL_c - 4M_{AE}PL_c\right) \end{array} \right) \\
&\quad + S.\left(M_{AE}^2 + M_{BC}^2 + \kappa_b.\left(M_{AE}^2 + M_{BC}^2\right)\right) + T.\left(-\frac{PL_c}{2} + M_{AE} + M_{BC}\right)^2
\end{aligned}
$$

(73)

where R, κ_c, and μ_c are modification coefficients that simplify the column's strain energy, S and κ_b are modification coefficients simplifying the beams' strain energies, and T is a modification coefficient for the strain energy of the half-elliptic bracing member:

$$
R = \frac{L_c}{6EI_c}, \kappa_c = \frac{7.8\alpha_c r_c^2}{L_c^2}, \mu_c = \frac{3r_c^2}{4L_b^2}
$$

(74)

$$
S = \frac{L_b}{12EI_b}, \kappa_b = \frac{31.2\alpha_b r_b^2}{L_b^2}
$$

(75)

$$
T = \frac{a.\lambda_{bav}}{EA_q L_c^2}
$$

(76)

According to Castigliano's second theorem, in a structure with linear elastic behavior, without temperature variation and support settlement, if the stored strain energy is obtained based on effective node forces or concentrated node moments, the partial derivative of the strain energy with respect to each of the effective forces exerted on the structure produces the displacement in that direction. Moreover, the partial derivative of the energy function with respect to each concentrated moment is the structure's rotation

Fig. 9 $\lambda_{bav}(e)$ as a function of parameter e assuming constant $\alpha_q = 2$
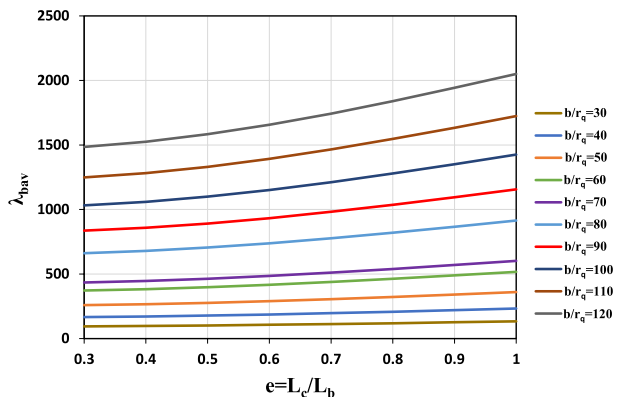
corresponding to that moment (Hibbeler and Kiang 2015). According to this theorem and Eq. (73), we can write for nodes A and B:

$$
\begin{aligned}
\Delta\theta_A = \frac{\partial U}{\partial M_{AE}} = 0 \rightarrow\ & R.\left(2M_{AE} - M_{BC} + \kappa_c.(2M_{AE} + 2M_{BC})\right. \\
& + \mu_c.\left(8M_{AE} - 4PL_c - 8M_{BC}\right)\left) + S.\left(2M_{AE} + \kappa_b.\left(2M_{AE}\right)\right) \right. \\
& + T.\left(2M_{AE} + 2M_{BC} - PL_c\right) = 0
\end{aligned}
\tag{77}
$$

$$
\begin{aligned}
\Delta\theta_B = \frac{\partial U}{\partial M_{BC}} = 0 \rightarrow\ & R.\left(2M_{BC} - M_{AE} + \kappa_c.(2M_{BC} + 2M_{AE})\right. \\
& + \mu_c.\left(8M_{BC} + 4PL_c - 8M_{AE}\right)\left) + S.\left(2M_{BC} + \kappa_b.\left(2M_{BC}\right)\right) \right. \\
& + T.\left(2M_{BC} + 2M_{AE} - PL_c\right) = 0
\end{aligned}
\tag{78}
$$

Solving the system of Eqs. (77) and (78) yields the unknown moments M_{AE} and M_{BC} to a good approximation:

$$
M_{AE} = M_{BC} \approx \eta P
\tag{79}
$$

In this equation:

$$
\eta = \frac{L_c\left(4\mu_c R + T\right)}{R\left(1 + 4\kappa_c\right) + 2S\left(1 + \kappa_b\right) + 4T}
\tag{80}
$$

The strain energy of the braced half-frame was obtained by substituting Eq. (79) in Eq. (73):

$$
\begin{aligned}
U = & R.\left(\eta^2 P^2 + \kappa_c.\left(4\eta^2 P^2\right) + \mu_c.\left(P^2 L_c^2\right)\right) + S.\left(2\eta^2 P^2 + \kappa_b\left(2\eta^2 P^2\right)\right) \\
& + T.\left(-\frac{PL_c}{2} + 2\eta P\right)^2
\end{aligned}
\tag{81}
$$

First, using Castigliano's second theorem and based on Eq. (81), the frame's horizontal displacement $\left(\Delta_x = 2\Delta_{Cx}\right)$ was obtained for calculating the stiffness of the quasi-X braced moment frame:

$$
\begin{aligned}
\Delta_x = 2\frac{\partial U}{\partial P} = & R \cdot \left(4\eta^2 P + \kappa_c \cdot \left(16\eta^2 P\right) + \mu_c \cdot \left(4PL_c^2\right)\right) \\
& + S \cdot \left(8\eta^2 P + \kappa_b\left(8\eta^2 P\right)\right) + T \cdot \left(PL_c^2 - 8\eta PL_c + 16\eta^2 P\right)
\end{aligned}
\tag{82}
$$

Substituting Eqs. (80) in (82), we have:

$$
\Delta_x = PL_c^2\left(\frac{\left(4\mu_c R + T\right)\left(R\left(1 + 4\kappa_c + 16\mu_c\right) + 2S\left(1 + \kappa_b\right)\right)}{R\left(1 + 4\kappa_c\right) + 2S\left(1 + \kappa_b\right) + 4T}\right)
\tag{83}
$$

Then, the elastic stiffness of the quasi-X-braced steel moment frame under lateral load P was obtained as expressed in Eq. (83):

$$
K = \frac{P}{\Delta_x} = \frac{R\left(1 + 4\kappa_c\right) + 2S\left(1 + \kappa_b\right) + 4T}{L_c^2\left(4\mu_c R + T\right)\left(R\left(1 + 4\kappa_c + 16\mu_c\right) + 2S\left(1 + \kappa_b\right)\right)}
\tag{84}
$$

β and γ were defined (Eqs. (75) and (76)) to simplify the stiffness relation:

$$\beta = \frac{I_b}{I_c} \tag{85}$$

$$\gamma = \frac{T}{S} = \frac{\frac{a.\lambda_{bav}}{EA_qL_c^2}}{\frac{L_b}{12EI_b}} = \frac{6I_b\lambda_{bav}}{A_qL_c^2} \tag{86}$$

Moreover, the ratio of R to S was obtained based on Eqs. (74) and (75) and substituting Eqs. (1) and (85) in these equations:

$$\frac{R}{S} = \frac{\frac{L_c}{6EI_c}}{\frac{L_b}{12EI_b}} = \frac{2L_c}{L_b} \times \frac{I_b}{I_c} = 2e\beta \tag{87}$$

Factorization by S in the numerator and the denominator of Eq. (84) and substituting Eqs. (76), (86), and (87) in the equation yielded the final stiffness:

$$
\begin{aligned}
K &= \frac{\left(\frac{R}{S}\right)\left(1+4\kappa_c\right) + 2\left(1+\kappa_b\right) + 4\left(\frac{T}{S}\right)}{SL_c^2\left(4\mu_c\left(\frac{R}{S}\right) + \left(\frac{T}{S}\right)\right)\left(\left(\frac{R}{S}\right)\left(1+4\kappa_c + 16\mu_c\right) + 2\left(1+\kappa_b\right)\right)} \\
&= \frac{2EA_q\gamma\left((2e\beta)\left(1+4\kappa_c\right) + 2\left(1+\kappa_b\right) + 4\gamma\right)}{L_b.\lambda_{bav}\left(\left(4\mu_c(2e\beta) + \gamma\right)\left((2e\beta)\left(1+4\kappa_c + 16\mu_c\right) + 2\left(1+\kappa_b\right)\right)\right)}
\end{aligned} \tag{88}
$$

By simplifying Eq. (88) using Eqs. (1), (85), (86) and assuming the columns' axial deformation to be negligible $\left(\mu_c \approx 0\right)$, we have:

$$K = K_{frame,bv} + K_{brace,bav} = \frac{24EI_c}{L_c^3}\left(\frac{e\beta}{(e\beta)\left(1+4\kappa_c\right) + \left(1+\kappa_b\right)}\right) + \frac{2EA_q}{L_b.\lambda_{bav}} \tag{89}$$

where the first phrase of the steel moment frame's stiffness takes into account bending, and shear deformations, and the second phrase is the stiffness of the quasi-X brace considering bending, shear, and axial deformations. Assuming the effects of shear and axial deformation in the beams and columns of the steel moment frame to be negligible $\left(\kappa_c = \kappa_b = \mu_c \approx 0\right)$, the elastic stiffness of the quasi-X-braced steel moment frame can be expressed by Eq. (88):

$$K = \frac{2EA_q(e\beta + 1 + 2\gamma)}{L_b.\lambda_{bav}(e\beta + 1)} \tag{90}$$

Simplifying Eq. (90) using Eqs. (1), (85), and (86), we have:

$$K = K_{frame,b} + K_{brace,bav} = \frac{24EI_c}{L_c^3}\left(\frac{e\beta}{1+e\beta}\right) + \frac{2EA_q}{L_b.\lambda_{bav}} \tag{91}$$

ρ was introduced (Eq. (90)) to normalize (nondimensionalize) stiffness:

$$\rho\left(e, \beta, \gamma, \frac{b}{r_q}, \alpha_q\right) = \frac{K}{\frac{EA_q}{L_b}} = \frac{2(e\beta + 1 + 2\gamma)}{\lambda_{bav}(e\beta + 1)} \tag{92}$$

Accordingly, with knowledge of the geometric specifications of the cross-sections of the columns, the beams, and the bracing members, as well as the material properties, Eq. (89) can be used to calculate the QXB-MF and QIXB-MF systems stiffness under lateral loading by a novel method accurately; The calculation's steps are as follows:

- Calculation of e (ratio of the half of the column's length to half of the beam's length) according to Eq. (1).
- Calculation of β (ratio of the second moment of area of the beam's strong axis to that of the column) according to Eq. (85).
- Calculation of γ (ratio of the modification coefficients of the quasi-X-bracing member to those of the beams) according to Eq. (86).
- Calculation of λ_{bav} according to Eq. (69) or Fig. 9.
- Calculation of modification coefficients κ_c and μ_c by inserting the columns specifications in Eq. (74).
- Calculation of modification coefficient κ_b by inserting beams specifications in Eq. (75).
- Calculation of elastic stiffness of the QXB-MF and QIXB-MF systems according to Eq. (89).

2.5 Calculating the elastic lateral stiffness of quasi-X-braced steel simple frames

This method can be used to find the elastic lateral stiffness of quasi-X-braced steel simple frames (QXB-SFs) and quasi inverse-X-braced steel simple frames (QIXB-SFs), too. Accordingly, the axial elastic stiffness of an element equivalent to the quarter-elliptic bracing member was calculated under an axial load of F (Fig. 10). This relation and spring modeling concepts were then used to calculate the quasi-X-braced frame's stiffness under lateral loading. The strain energy stored in the quarter-elliptic bracing member is calculated by Eq. (67) as follows:

$$U_{quarter-elliptic\ brace,\ bav} = \frac{F^2.a}{2EA_q} \cdot \frac{\lambda_{bav}}{1 + e^2} \tag{93}$$

The stiffness of the equivalent element of the quarter-elliptic bracing member was first obtained using Castigliano's second theorem by calculating the axial displacement $\left(\Delta_e\right)$ from Eq. (93):

$$\Delta_e = \frac{\partial U}{\partial F} = \frac{F.a}{EA_q} \cdot \frac{\lambda_{bav}}{1 + e^2} \tag{94}$$

Then, based on Eqs. (1) and (94), the elastic axial stiffness of the equivalent element of the quarter-elliptic bracing member under the axial load F can be obtained as follows:

$$K_e = \frac{F}{\Delta_e} = \frac{2EA_q\left(1 + e^2\right)}{L_b.\lambda_{bav}} \tag{95}$$

Drawing on the concepts of spring modeling, for a two-dimensional single-span and one-story simple frame equipped with quasi-X brace under lateral force, the elastic lateral stiffness can be obtained as follows:

$$K = 2\left(\frac{K_e \cos^2 \theta}{2}\right) = K_e \cos^2 \theta = \frac{2EA_q}{L_b \cdot \lambda_{bav}} \tag{96}$$

Accordingly, with knowledge of the geometric specifications of the cross-sections of the columns, the beams, and the bracing members, as well as the material properties, Eq. (96) can be used to calculate the QXB-SF and QIXB-SF systems stiffness under lateral loading by a novel method accurately.

2.6 Developing the proposed formulation for special cases of the QXB-MF systems

Equation (91) shows the elastic stiffness of the two-dimensional single-span and one-story quasi-X-braced steel moment frame under a lateral load of P, assuming negligible shear and axial deformation in the beams and columns. The relation was developed in the structural frames considering two different beam conditions. In the first case, all beams in the moment frame are assumed to be rigid $\left(\beta = I_b/I_c = \infty\right)$, whereas they are elastic in the second case.

- In the first case, for a QXB-MF system with a total of n_1 spans, n_2 of which are equipped with quasi-X brace, and m_1 stories, and considering rigid beams with infinite bending stiffness, the lateral stiffness under a load of P applied on the top-most story can be calculated from the equation in Table 1(a). In this case, supports of all columns are rigid and undergo no rotation at the beam-to-column connection. Therefore, in this special case, the column behaves similar to a beam with one fixed support and one sliding support with stiffness of $12EI_c/L_c^3$. The lateral load is then divided between the columns and quasi-X brace that sustain equal deformations, allowing them to behave similarly to parallel springs, the lateral stiffness of which can be summed up according to spring modeling principles. Moreover, spring modeling principles allow the lateral stiffness of the story to be combined similarly to springs arranged in series.

Fig. 10 Equivalent element for the quarter-elliptic bracing member
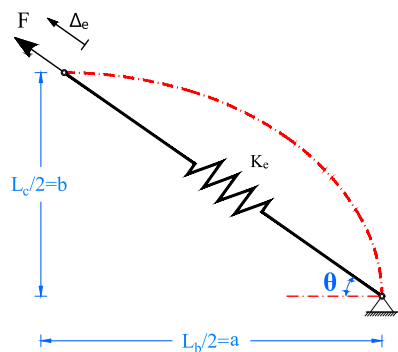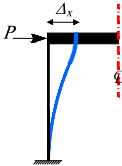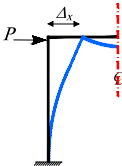
- In the second case, for a QXB-MF system with a total of n_1 spans $\left(n_1=2^N\right)$, n_2 of which are equipped with quasi-X brace, and considering elastic beams, the lateral stiffness under a load of P applied on the top-most story can be calculated from the equation in Table 1(b). The lateral load is then divided between the moment frame and quasi-X brace that sustain equal deformations, allowing them to behave similarly to parallel springs, the lateral stiffness of which can be summed up according to spring modeling principles.

3 Validating the accuracy of the elastic stiffness formulation for QXB-MFs by finite-element modeling

In total, 1600 two-dimensional single-span and one-story quasi-X-braced steel moment frames were modeled under a 10,000 N lateral load in OpenSees to control and validate the accuracy of the elastic stiffness formulation derived from strain energy and Castigliano's theorem (Mazzoni et al. 2006; Hibbeler and Kiang 2015). In these frames, the columns and beams were 3,000 and 5,000 mm long, and the cross-sectional area and the second moment of area of the bending (strong) axis of the quasi-X-braced member were 2256 mm^2 and 33.35×10^5 mm^4, respectively. The elastic beam-column element was used for all members of the frames. Moreover, uniaxial elastic materials were used to simulate steel's behavior in the frames. Forty different values were assigned to β (ratio of the second moment of area of the beam's strong axis to that of the column) using MATLAB programming code and based on Eq. (85), whereas γ (ratio of the correction factors of the quasi-X-bracing member and the beams) was assigned 40 different values in the model developed using Open-Sees according to Eq. (86), obtaining the displacement of 1600 QXB-MF systems. Then, using the stiffness relation and considering a 10,000 N lateral load, the frames' elastic stiffness was calculated. In this section, because the results of the two systems, QXB-MF and

Table 1 Special cases of elastic lateral stiffness in QXB-MF systems

Case	Beam condition	Deflected shape	Lateral stiffness
a	Rigid beam		$K = \frac{1}{m_1}\left[(n_1+1)\left(\frac{12EI_c}{L_c^3}\right) + n_2\left(\frac{2EA_q}{L_b.\lambda_{bav}}\right)\right]$
b	Elastic beam*		$K = n_1\left(\frac{24EI_c}{L_c^3}\left(\frac{e\beta}{1+e\beta}\right)\right) + n_2\left(\frac{2EA_q}{L_b.\lambda_{bav}}\right)$

*For single-story and even-span $\left(n_1=2^N\right)$ frames

QIXB-MF, are almost identical, only the results and diagrams of the QXB-MF system are presented.

Figure 11a plots the normalized stiffness (ρ) of the QXB-MF system against different ratios of modification coefficients of the quasi-X-bracing member and beams (γ) and different ratios of second moment of area of the strong axis of the beam to that of the column (β). With the software tool unable to consider the shear shape coefficient of the quasi-X bracing member's cross-section (α_q) due to using elastic beam-column elements, this parameter was assumed to be 0. The diagrams were plotted for 40 different values of γ between 0.5 and 20, and 40 different values of β between 0.05 and 2. For simplification, Fig. 11a shows only nine out of 40 plots of the different β values between 0.05 and 2. According to Fig. 11a, the normalized stiffness variations (ρ) in the QXB-MF system rose linearly against the ratio of the modification coefficients of the quasi-X bracing member and the beams (γ), as well as the ratio of the second moment of area of the strong axis of the beam to that of the column (β), as γ increased. Figure 11b shows the normalized stiffness (ρ) of the QXB-MF system against different moments of inertia of the beam's strong axis to those of the columns (β) and for different ratios of the modification coefficients of the quasi-X bracing members to that of the beams (γ). These graphs were plotted for 40 different γ values between 0.5 and 20 and 40 different β values between 0.05 and 2, considering the shear shape coefficient of the quasi-X bracing cross-section (α_q) to be 0. For simplification, Fig. 11b shows only nine out of 40 plots of the different γ values between 0.5 and 20. According to Fig. 11b, the normalized stiffness of the QXB-MF system declined as the second moment of area of the strong axis of the column decreased relative to that of the beam (increase in β).

Assuming the ratio of the second moment of area of the beam's strong axis to that of the column (β) to be 1, the QXB-MF system's normalized stiffness (ρ) was calculated for 40 different γ values between 0.5 and 20 from Eq. (92) and plotted in Fig. 12a. This figure was also plotted considering the shear shape coefficient of the quasi-X-bracing cross-section (α_q) to be 0 in Eq. (69). Assuming the ratio of the modification coefficients of the quasi-X-bracing member to those of the beams to be 10, the QXB-MF system's normalized stiffness (ρ) was calculated for 40 different β values between 0.05 and 2 from Eq. (92) and plotted in Fig. 12b. This figure was also plotted considering the shear shape coefficient of the quasi-X-bracing cross-section (α_q) to be 0 in Eq. (69). Figure 12 is suggestive of negligible error between the results of the proposed formulation and finite element analysis.
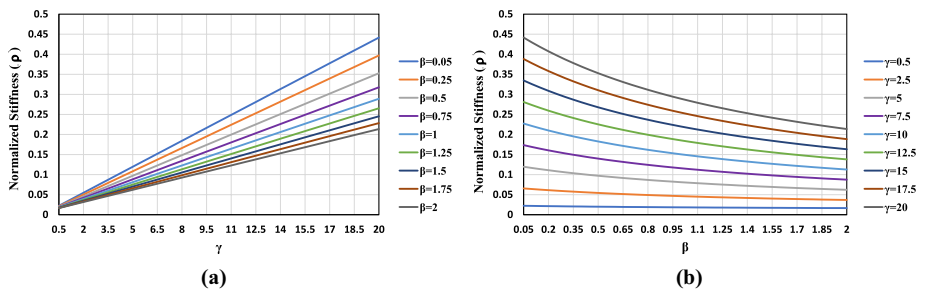
Fig. 11 Changes in normalized stiffness of the QXB-MF system (ρ); **a** versus parameter γ for different values of β, **b** versus parameter β for different values of γ

4 Numerical example for the QXB-MF and QIXB-MF system's elastic stiffness

This section evaluates and validates the accuracy of the proposed formulation for the lateral stiffness of QXB-MF and QIXB-MF systems through numerical examples. For this purpose, two-dimensional one-story and single-span frames were modeled in SAP 2000 and Abaqus software (Simulia 2014). The columns and beams were 3,000 and 5,000 mm long in these frames, and a 10,000 N lateral load was applied (Fig. 13).

The HEB 300 section was used for the columns, the IPE 300 section for the beams, and the BOX $100 \times 100 \times 6$ for the bracing members. Table 2 lists the details of these sections. In the table, A denotes the cross-section area, I_x and r_x are the second moment of area and the radius of gyration of the section around the bending (strong) axis, and α represents the cross-section's shear shape coefficient.

For better modeling of the quasi-X brace in SAP 2000 software, each quarter-elliptic member of the bracing was divided into ten equal parts. The element of choice to model the frame members in Abaqus software was the B21 (beam element), which is a two-dimensional element with two nodes that come with two translational degrees of freedom and one rotational degree of freedom. Moreover, Multi-point constraints (MPCs) connections were used as pinned connections in the quasi-X bracing members. Table 3 (EN1993-1–1) presents the properties of the S235JR steel that was used in all components (EN 1993-1-1 2005).

First, the lateral displacement of the studied frames was obtained in both software tools (Fig. 14 and Fig. 15). Then, using the stiffness formulation and considering a 10,000 N lateral load, the frames' elastic stiffness was calculated using Eqs. (97) and (98).

The QXB-MF and QIXB-MF systems' lateral stiffness was obtained using Abaqus software (Fig. 14):

$$K = \frac{P}{\Delta} = \frac{10000}{1.283} = 7794.23 \frac{N}{mm} \tag{97}$$

The QXB-MF and QIXB-MF systems' lateral stiffness was obtained using SAP 2000 software (Fig. 15):

$$K = \frac{P}{\Delta} = \frac{10000}{1.271} = 7867.82 \frac{N}{mm} \tag{98}$$
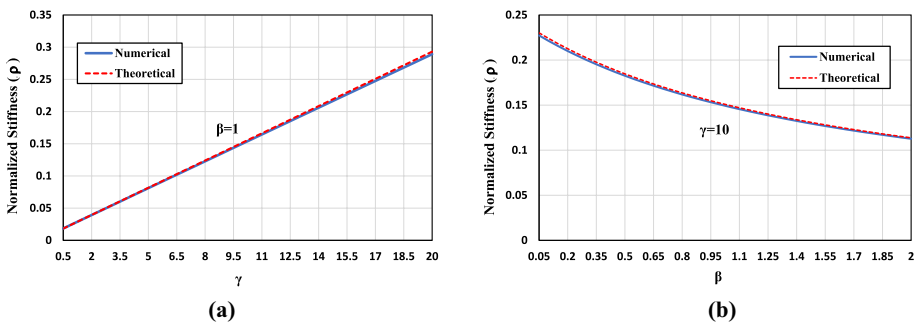
Fig. 12 Comparison of the results obtained by the numerical models and Eq. (92) for ρ; **a** versus parameter γ assuming constant $\beta = 1$, **b** versus parameter β assuming constant $\gamma = 10$

Moreover, the QXB-MF and QIXB-MF systems' lateral stiffness was calculated using the proposed formulation (Table 4).

Comparing the analysis results of the two finite element tools for the QXB-MF and QIXB-MF systems with the proposed formulation indicated an error level of below 1%, which can be attributed to the shear shape coefficient of the cross-sections (α). Assuming the shear shape coefficient to be zero results in a negligible difference between the results.

5 Seismic performance evaluation of the QXB-MF and QIXB-MF systems

This section assesses the seismic performance of the QXB-MF and QIXB systems. Two single-span and single-story frames from the three-dimensional archetypes designed in the seismic design category (SDC) D_{max} with a response modification factor of 5 have been chosen. S235JR steel is utilized for all cross-sections, and the gravitational dead and live loads for these archetypes are taken into account to be 500 kgf/m^2 and 200 kgf/m^2, respectively. OpenSees software has been used to perform nonlinear modeling, which conforms to FEMA P695 modeling and analysis requirements (FEMA P695 2009). In order to demonstrate the softening and deterioration of the studied frames, concentrated plastic hinge modeling is employed. In this method, plastic hinges are positioned at both ends of the columns and beams, and the middle element is modeled elastically. Quarter-elliptic members with twelve elements and five plastic hinges are modeled, so a plastic hinge is placed at one end of each element. The panel zone in moment frame systems was modeled using the
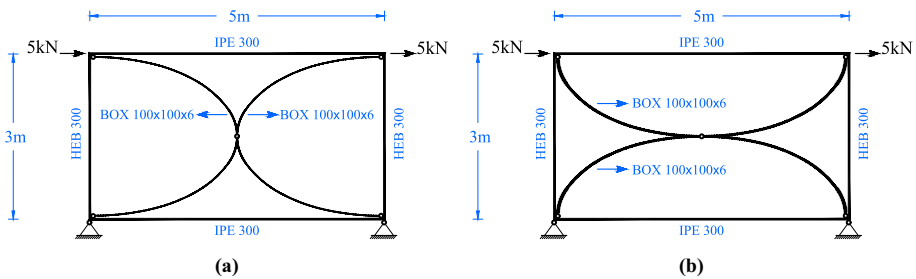
Fig. 13 Modeling of the two-dimensional single-story single-span frames; **a** QXB-MF, **b** QIXB-MF

Section properties	HEB 300	IPE 300	BOX 100×100×6
$A\,(mm^2)$	14,900	5380	2256
$I_x\,(mm^4)$	2517×10^5	836×10^5	33.36×10^5
$r_x\,(mm)$	130	125	38.45
$\alpha = A/A'$	4.25	2.48	2

Table 2 Section properties

Standard and Steel grade	$t \leq 40mm$			
	$F_y[N/mm^2]$	$F_u[N/mm^2]$	$E[N/mm^2]$	ν
S235JR	235	360	210,000	0.3

Table 3 Material properties
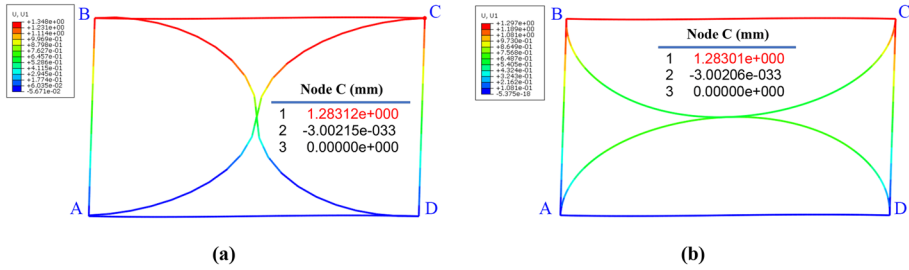
Fig. 14 Elastic displacement of frames subjected to lateral force (Abaqus)
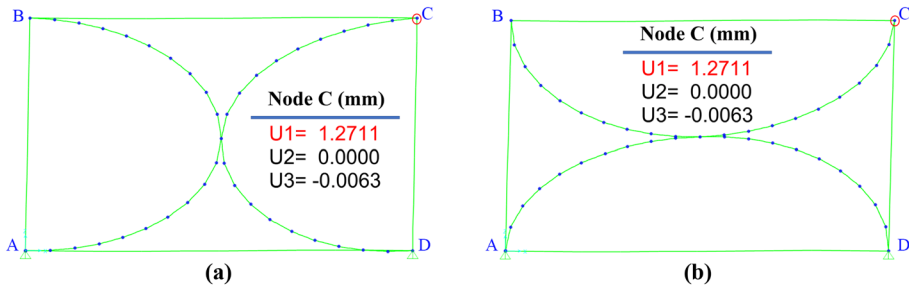
Fig. 15 Elastic displacement of frames subjected to lateral force (SAP 2000)

eight-element Krawinkler model (NIST 2017). As shown in Fig. 16, HEB 140, IPE 200, and BOX $100 \times 100 \times 10$ cross-sections were utilized for columns, beam, and quarter-elliptic bracing members, respectively. The moment-rotation behavior of the concentric hinges is simulated by the modified Ibarra-Medina-Krawinkler (IMK) deterioration model with a bilinear hysteretic response in all members (Lignos and Krawinkler 2010, 2011; Lignos et al. 2019).

To assess the seismic performance of the QXB-MF and QIXB-MF systems, non-linear static analysis (pushover) and incremental dynamic analysis (IDA) are conducted on the moment frame with quasi-X braces and the moment frame without brace (IMF), and the outcomes are compared.

5.1 Non-linear static analysis (pushover)

Pushover analysis is carried out under lateral static loads and gravity loads. The structure is initially subjected to gravity loads, and subsequently, it is subjected to the lateral loading pattern. As per FEMA P695, in the pushover analysis, gravity load is applied to the structure through the load combination in Eq. (99):

$$1.05D + 0.25L \tag{99}$$

where D is the nominal dead load, and L is the nominal live load. The above equation coefficients signify the expected values of loads with normal probability distribution. Then, the distribution of the lateral force equivalent to the earthquake at the structure's height based on the structure's first mode and the effective mass of the floors is conducted through Eq. (100):

Table 4 Lateral stiffness of QXB-MF and QIXB-MF using the proposed formulation

No.	Equation or Figure number	Parameters	Calculation of the parameter(s)
1	Equation (1)	e	0.6
2	Equation (85)	β	0.332
3	Equation (86)	γ	4.425
4	Equation (74)	κ_c and μ_c	$\kappa_c = 0.0622$ $\mu_c = 0.0005$
5	Equation (75)	κ_b	$\kappa_b = 0.0483$
6	Equations (58), (62) and (66) or Fig. 8	$\lambda_b(e), \lambda_a(e)$ and $\lambda_v(e)$	$\lambda_b(e) = 0.0852$ $\lambda_a(e) = 1.079064$ $\lambda_v(e) = 0.197287$
7	Equation (69) or Fig. 9	$\lambda_{bav}(e)$	179.2
8	Equation (88)	K	$7859.75 N/mm^2$
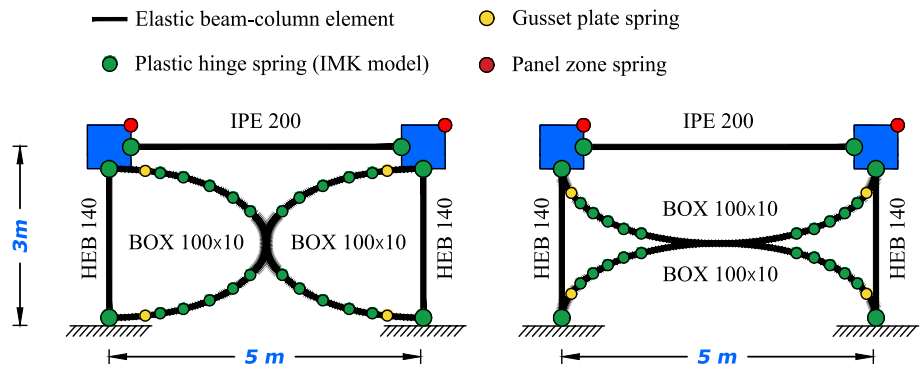
Fig. 16 QXB-MF and QIXB-MF systems modeling approach in OpenSees

$$F_x \propto m_x \varphi_{1,x} \tag{100}$$

where F_x is the lateral force distribution in height at each floor level (x), m_x is the structure's mass at level x, and $\varphi_{1,x}$ is the first mode of the structure at level x. The pushover curve of QXB-MF, QIXB-MF, and IMF archetypes is illustrated in Fig. 17. In this figure, V_{max}/w is equal to the maximum amount of base shear normalized by weight, δ_u is equal to the roof displacement at the point where 20% of the maximum base shear is reduced, and $\delta_{y,eff}$ is the effective yield displacement of the roof calculated as per FEMA P695 guidelines (FEMA P695 2009).

According to Eq. (101), the over-strength factor, Ω, is equal to the ratio of the maximum base shear (V_{max}) to the design base shear(V):

$$\Omega = \frac{V_{max}}{V} \tag{101}$$

Furthermore, according to Eq. (102), period-based ductility, μ_T, is equal to the ratio of the ultimate displacement of the roof (δ_u) to the effective yield displacement of the roof ($\delta_{y,eff}$):

$$\mu_T = \frac{\delta_u}{\delta_{y,eff}} \tag{102}$$

Comparing the pushover curves depicted in Fig. 17 reveals that incorporating quasi-X braces into the moment frame system has resulted in performance enhancements, increased elastic stiffness, increased maximum base shear, and increased ultimate displacement capacity of this structural system.

5.2 Incremental dynamic analysis (far-field and near-field ground motion records)

The median collapse capacity and safety margin are determined using incremental dynamic analysis and based on the FEMA P695 approach for evaluating the seismic performance of structures (FEMA P695 2009). In this study, the selected parameters for damage measure (DM) and intensity measure (IM), respectively, are maximum inter-story drift ratio (MIDR) and first mode-5% damped spectral acceleration, $S_a(T_1, 5\%)$. The median collapse capacity of each structure, $\hat{S}_{CT}$, is computed through IDA analysis under specific records, and the collapse margin ratio (CMR) is determined as follows:

$$CMR = \frac{\hat{S}_{CT}}{S_{MT}} \tag{103}$$

where S_{MT} is the maximum considered earthquake (MCE) ground motion intensity. Conforming to FEMA P695 and based on the structural period (T_1) and SDC D$_{max}$, this value is calculated as 1.5 for the studied archetypes. To consider the effects of frequency content (spectral shape) and adjust the records utilized, the CMR index is multiplied by a parameter called the spectral shape factor (SSF) to acquire the adjusted collapse margin ratio (ACMR). SSF values are computed through FEMA P695 tables based on T_1 and μ_T.

$$ACMR = CMR \times SSF \tag{104}$$

The requirements for acceptance of the structural systems' collapse performance rely on all uncertainties applied in the evaluation process. These uncertainties comprise record-to-record uncertainty (β_{RTR}), modeling uncertainty (β_{MDL}), test data uncertainty (β_{TD}), and design requirements uncertainty (β_{DR}). As per FEMA P695, quality level A (equal to 0.2) was selected in this study for the β_{MDL}, β_{TD}, and β_{DR} uncertainties. β_{RTR} is considered equal to 0.4 for structures with μ_T greater than 3, and for structures with μ_T smaller than 3, the following equation is utilized to determine this uncertainty:

$$0.2 \leq \beta_{RTR} = 0.1 + 0.1\mu_T \leq 0.4 \tag{105}$$

Because the four mentioned uncertainty sources are independent of each other, their total standard deviation is geometrically added to acquire the total collapse uncertainty (β_{TOT}):

$$\beta_{TOT} = \sqrt{\beta_{RTR}{}^2 + \beta_{MDL}{}^2 + \beta_{TD}{}^2 + \beta_{DR}{}^2} \tag{106}$$

In order to compare the seismic performance of QXB-MF, QIXB-MF, and IMF archetypes under the effects of far-field and near-field ground motion records, the set of records proposed by FEMA P695, including 22 pairs of far-field records and 28 pairs
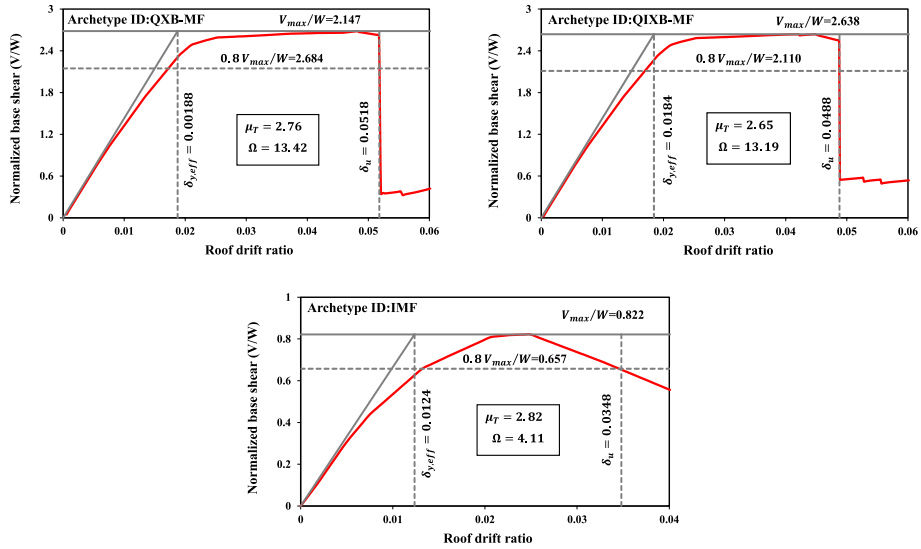
Fig. 17 Pushover curves of archetypes

of near-field records (with and without pulses), is utilized. Additionally, the advanced "hunt and fill" algorithm was employed to carry out an optimal and intelligent scale for the intensity measure (Vamvatsikos and Cornell 2002). In this algorithm, values of 0.05, 0.05, and 30 were assigned to the initial step, step increment, and allowed number of runs per record, respectively. Figure 18 illustrations IDA curves with 16%, 50%, and 84% fractile curves under 44 far-field records, and Fig. 19 demonstrations IDA curves with 16%, 50%, and 84% fractile curves under 56 near-field records. According to the FEMA P695 tables, the acceptable collapse margin ratios ($ACMR_{10\%}$) for QXB-MF, QIXB-MF, and IMF archetypes are 1.92, 1.91, and 1.93, respectively. Consequently, the criterion $ACMR > ACMR_{10\%}$ has been satisfied per archetype.

Comparing the IDA curves reveals that using these braces in moment frame systems increases $\hat{S}_{CT}$, which in turn increases ACMR and improves the seismic performance of these systems. Using quasi-X braces increases the ACMR by 64.17% for far-field ground motion records and 126.42% for near-field ground motion records in the moment frame system. Also, using quasi inverse-X braces increases the ACMR by 50.79% for far-field ground motion records and 95.28% for near-field ground motion records in the moment frame system. The better seismic performance during near-field ground motion records is caused by longer periods of these records than the studied systems' periods.

5.3 Collapse fragility evaluation

The fragility curves exhibit the collapse probability of structures for different intensity measures. They indicate the collapse probability per spectral acceleration level. The fragility curves are drawn using a cumulative distribution function (CDF) from IDA results. The lognormal collapse fragility is specified by two main factors: the median collapse intensity
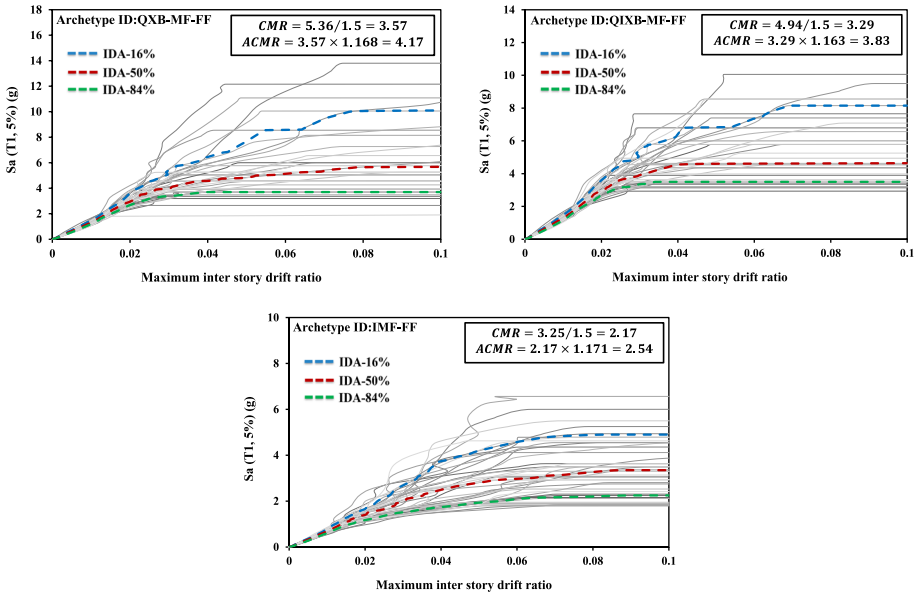
Fig. 18 IDA curves of archetypes under far-field ground motion records
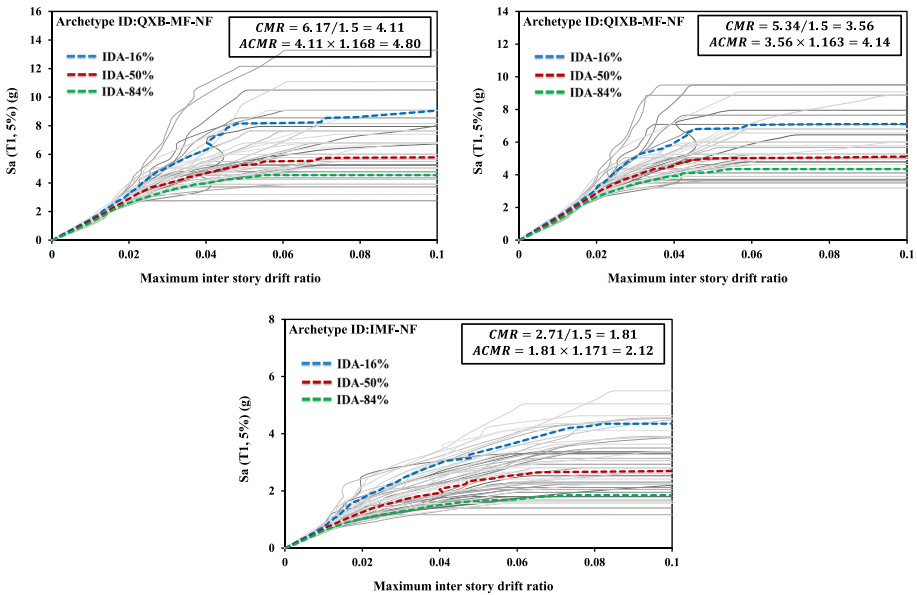
Fig. 19 IDA curves of archetypes under near-field ground motion records

$\left(\widehat{S}_{CT}\right)$ and the standard deviation of the natural logarithm. Figure 20 depicts the fragility curve for archetypes under far-field records, and Fig. 21 depicts the fragility curve for archetypes under near-field records.
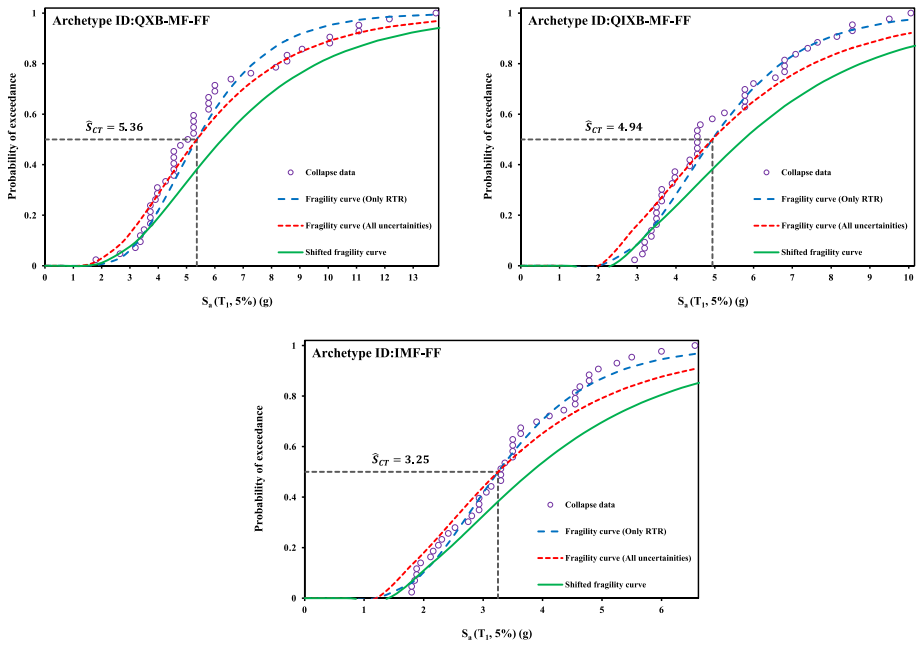
Fig. 20 Fragility curves of archetypes under far-field ground motion records
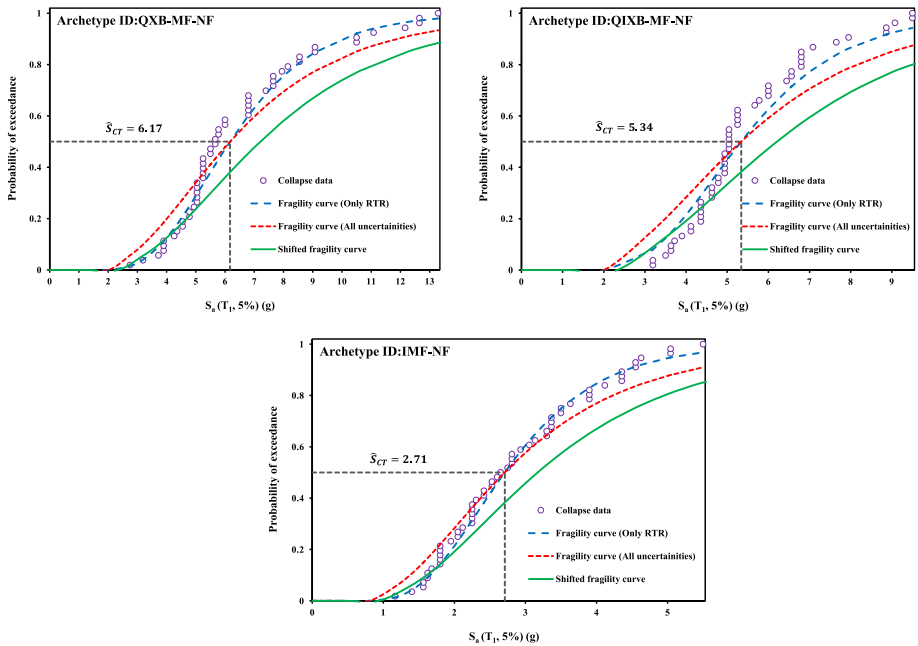
Fig. 21 Fragility curves of archetypes under near-field ground motion records

In these figures, two dashed fragility curves are drawn by considering β_{RTR} and β_{TOT} (all uncertaintiesas) the standard deviation parameter in the lognormal cumulative distributive function. Additionally, the solid curve (shifted fragility curve) is drawn by multiplying the fragility curve with the standard deviation parameter β_{TOT} in SSF. The fragility curve slope has increased with the median collapse intensity $\left(\hat{S}_{CT}\right)$ increase and the standard deviation increase.

6 Conclusions

This study introduces the novel quasi-X braces that are intended to correct conventional CBFs. Novel analytical and numerical methods evaluated the stiffness and stability of the quasi-X-braced steel moment frames. For this purpose, first, a new and accurate analytical formulation was presented for the lateral elastic stiffness of the two-dimensional single-span and one-story QXB-MF and QIXB-MF systems under lateral loading, considering all effective parameters, including the axial and shear loads and the bending moment for all frame members. Next, the accuracy of the relation was evaluated by modeling the QXB-MF and QIXB-MF systems using OpenSees and assigning 40 different values to the ratio of the second moments of area of the beam's and column's strong axes and 40 values to the ratio of the correction factors of the quasi-X bracing member and the beams using MATLAB programming code. Moreover, two finite element software tools were used to solve the numerical problems to compare the results with the proposed relation. The error was found to be less than 1%, showing the high accuracy and reliability of the proposed relation. Accordingly, knowledge of the geometric specifications of the columns, beams, and the quasi-X bracing members, as well as material properties, helps calculate the elastic stiffness of the QXB-MF and QIXB-MF systems under lateral loading easily by relying on sufficient conservative considerations and by taking into account the uncertainties. these systems' seismic performance was assessed as per the FEMA P695 guidelines under far-field and near-field ground motion records in comparison with the IMF system. Initially, pushover analysis was performed on the archetype structures, resulting in the determination of period-based ductility and over-strength factors derived from the pushover curves. Subsequently, IDA analysis was performed using 44 far-field and 56 near-field ground motion records, and fragility curves were drawn using the collapse data. Comparing the obtained results reveals that including quasi-X braces in the IMF system increases the ACMR (adjusted collapse margin ratio) by 1.5 times for far-field ground motion records and 2 times for near-field ground motion records, consequently improving this system's seismic performance.

Declarations

Conflict of interest The authors have no relevant financial and non-financial interests to disclose.

Informed consent All authors named on the submission of this paper, made significant contributions throughout the preparation of the work and agree to be accountable for all aspects of the work, and also will be fully responsible to any obscure part mentioned by revered peer reviewers.

References

Afsar Dizaj E, Fanaie N, Zarifpour A (2018) Probabilistic seismic demand assessment of steel frames braced with reduced yielding segment buckling restrained braces. Adv Struct Eng 21:1002–1020. https://doi.org/10.1177/1369433217737115

Andalib Z, Kafi MA, Kheyroddin A, Bazzaz M (2014) Experimental investigation of the ductility and performance of steel rings constructed from plates. J Constr Steel Res 103:77–88. https://doi.org/10.1016/j.jcsr.2014.07.016

Arzeytoon A, Toufigh V (2018) Experimental and numerical studies on ribbed bracing system. Struct Des Tall Spec Build 27:1–16. https://doi.org/10.1002/tal.1493

Bazzaz M, Kafi MA, Kheyroddin A et al (2014) Evaluating the seismic performance of off-centre bracing system with circular element in optimum place. Int J Steel Struct 14:293–304. https://doi.org/10.1007/s13296-014-2009-x

Bazzaz M, Andalib Z, Kafi MA, Kheyroddin A (2015a) Evaluating the performance of OBS-C-O in steel frames under monotonic load. Earthq Struct 8:699–712. https://doi.org/10.12989/eas.2015.8.3.699

Bazzaz M, Andalib Z, Kheyroddin A, Kafi MA (2015b) Numerical comparison of the seismic performance of steel rings in off-centre bracing system and diagonal bracing system. Steel Compos Struct 19:917–937. https://doi.org/10.12989/scs.2015.19.4.917

Cheraghi A, Zahrai SM (2019) Cyclic testing of multilevel pipe in pipe damper. J Earthq Eng 23:1695–1718. https://doi.org/10.1080/13632469.2017.1387191

Davis R, Henshell RD, Warburton GB (1972a) Constant curvature beam finite elements for in-plane vibration. J Sound Vib 25:561–576. https://doi.org/10.1016/0022-460X(72)90478-6

Davis R, Henshell RD, Warburton GB (1972b) Curved beam finite elements for coupled bending and torsional vibration. Earthq Eng Struct Dyn 1:165–175. https://doi.org/10.1002/eqe.4290010205

Dussault S (2012) Finite element analysis of ductile fuses for W-shape steel bracing members. 15th World Conf Earthq Eng

Ebadi P, Sabouri-Ghomi S (2012) Conceptual study of X-braced frames with different steel grades using cyclic half-scale tests. J Earthq Eng Eng Vib 11:313–329. https://doi.org/10.1007/sl1803-012-0124-2

EN 1993-1-1 (2005) Eurocode 3: Design of steel structures - Part 1-1: General rules and rules for buildings. European Committee for Standardisation, Brussels

Fanaie N, Dizaj EA (2014) Response modification factor of the frames braced with reduced yielding segment BRB. Struct Eng Mech 50:1–17. https://doi.org/10.12989/sem.2014.50.1.001

Fanaie N, Shirpour A (2023) Analytical and numerical evaluation of quarter-elliptic-braced steel moment frames (QEB-MFs). Structures 49:426–442. https://doi.org/10.1016/j.istruc.2023.01.100

Fanaie N, Sadegh Kolbadi M, Afsar Dizaj E (2017) Probabilistic Seismic Demand Assessment of Steel Moment Resisting Frames Isolated by LRB. Numer Methods Civ Eng 2:52–62. https://doi.org/10.29252/nmce.2.2.52

FEMA P695 (2009) Quantification of building seismic performance factors

Grande E, Rasulo A (2013) Seismic assessment of concentric X-braced steel frames. Eng Struct 49:983–995. https://doi.org/10.1016/j.engstruct.2013.01.002

Hibbeler RC, Kiang T (2015) Structural analysis. Pearson Prentice Hall Upper Saddle River

Horibe T, Mori K (2015) In-plane and out-of-plane deflection of J-shaped beam. J Mech Eng Autom 5(1):14–19. https://doi.org/10.5923/j.jmea.20150501.02

Ismail M (2019) An elastoplastic bracing system for structural vibration control. Eng Struct 200:109671. https://doi.org/10.1016/j.engstruct.2019.109671

Jouneghani HG, Haghollahi A (2020) Assessing the seismic behavior of steel moment frames equipped by elliptical brace through incremental dynamic analysis (IDA). Earthq Eng Eng Vib 19:435–449. https://doi.org/10.1007/s11803-020-0572-z

Jouneghani HG, Haghollahi A, Moghaddam H, Moghadam AS (2016) Study of the seismic performance of steel frames in the elliptic bracing. J Vibroeng 18:2974–2985. https://doi.org/10.21595/jve.2016.16858

Jouneghani HG, Haghollahi A, Beheshti-Aval SB (2020) Experimental study of failure mechanisms in elliptic-braced steel frame. Steel Compos Struct 37:175–191. https://doi.org/10.12989/scs.2020.37.2.175

Kachooee A, Kafi MA (2018) A suggested method for improving post buckling behavior of concentric braces based on experimental and numerical studies. Structures 14:333–347. https://doi.org/10.1016/j.istruc.2018.04.003

Kumar MS, Senthilkumar R, Sourabha L (2019) Seismic performance of special concentric steel braced frames. Structures 20:166–175. https://doi.org/10.1016/j.istruc.2019.03.012

Lee H-P (1969) Generalized stiffness matrix of a curved-beam element. AIAA J 7:2043–2045

Lignos DG, Krawinkler H (2011) Deterioration modeling of steel components in support of collapse prediction of steel moment frames under earthquake loading. J Struct Eng 137:1291

Lignos DG, Hartloper AR et al (2019) Proposed updates to the ASCE 41 nonlinear modeling parameters for wide-flange steel columns in support of performance-based seismic engineering. J Struct Eng 145:1–13. https://doi.org/10.1061/(ASCE)ST.1943-541X.0002353

Lignos DG, Krawinkler H (2010) A steel database for component deterioration of tubular hollow square steel columns under varying axial load for collapse assessment of steel structures under earthquakes. In: Proceedings of the 7th International conference on urban earthquake engineering (7CUEE)

Mahmoudi M, Mehrizi AZ, Shirpour A (2018) Evaluation of the effect of end-connection specifications on lateral bearing capacity of concentrically braced steel frames. Int J Steel Struct 18:179–187. https://doi.org/10.1007/s13296-018-0314-5

Mahmoudi M, Shirpour A, Zarezadeh A (2019) The Effects of mid-span connection specifications on compressive performance of cross (X) braces. Int J Steel Struct 19:1125–1133. https://doi.org/10.1007/s13296-018-0192-x

Marotta E, Salvini P (2018) Analytical stiffness matrix for curved metal wires. Procedia Struct Integr 8:43–55. https://doi.org/10.1016/j.prostr.2017.12.007

Mazzoni S, McKenna F, Scott MH, Fenves GL (2006) OpenSees command language manual. Pacific Earthq Eng Res Cent 264:137–158

Moghaddam HA, Estekanchi HE (1995) On the characteristics of an off-centre bracing system. J Constr Steel Res 35:361–376

Moghaddam HA, Estekanchi HE (1999) Seismic behaviour of offcentre bracing systems. J Constr Steel Res 51:177–196. https://doi.org/10.1016/S0143-974X(99)00007-3

Moradi Garoosi AR, TahamouliRoudsari M, Hosseini Hashemi B (2018) Experimental evaluation of rigid connection with reduced section and replaceable fuse. Structures 16:390–404. https://doi.org/10.1016/j.istruc.2018.11.010

NIST 2017b (2017) Guidelines for nonlinear structural analysis for design of buildings Part IIa–steel moment frames

Palaninathan R, Chandrasekharan PS (1985) Curved beam element stiffness matrix formulation. Comput Struct 21:663–669. https://doi.org/10.1016/0045-7949(85)90143-9

Payandehjoo B, Sabouri-Ghomi S, Ebadi P (2016) Seismic Behavior of X-shaped drawer bracing system (DBS) and X-braced frames with heavy central core. J Earthq Tsunami 10:1–28. https://doi.org/10.1142/S1793431116500044

Rao SS (1971) Effects of transverse shear and rotatory inertia on the coupled twist-bending vibrations of circular rings. J Sound Vib 16:551–566. https://doi.org/10.1016/0022-460X(71)90662-6

Roeder CW, Sen AD, Asada H et al (2020) Inelastic behavior and seismic design of multistory chevron-braced frames with yielding beams. J Constr Steel Res 167:105817. https://doi.org/10.1016/j.jcsr.2019.105817

Sabouri-Ghomi S, Payandehjoo B, Ghasemzadeh H (2017) Analytical approach of buckling strength of yielding damped braced core (YDBC). Numer Methods Civ Eng 1(4):32–37

Sen AD, Roeder CW, Lehman DE, Berman JW (2019) Nonlinear modeling of concentrically braced frames. J Constr Steel Res 157:103–120. https://doi.org/10.1016/j.jcsr.2019.02.007

Shirinkam MR, Razzaghi J (2020) Experimental and analytical investigation on the behavior of metallic Box-Shaped Dampers (BSD). Structures 23:766–778. https://doi.org/10.1016/j.istruc.2019.12.018

Simulia DS (2014) Abaqus 6.14 user's manual. Dassault Systems, Providence, RI

Taiyari F, Mazzolani FM, Bagheri S (2019) A proposal for energy dissipative braces with U-shaped steel strips. J Constr Steel Res 154:110–122. https://doi.org/10.1016/j.jcsr.2018.11.031

Vamvatsikos D, Cornell CA (2002) Incremental dynamic analysis. Earthq Eng Struct Dyn 31:491–514. https://doi.org/10.1002/eqe.141

Varughese K, El-Hacha R (2020) Design and behaviour of steel braced frame reinforced with NiTi SMA wires. Eng Struct 212:110502. https://doi.org/10.1016/j.engstruct.2020.110502

Yamada Y, Ezawa Y (1977) On curved finite elements for the analysis of circular arches. Int J Numer Methods Eng 11:1635–1651

Yang Y-B, Kuo S-R (1996) Discussion: thin-walled curved beams. I: formulation of nonlinear equations. j Eng Mech 122:482–484. https://doi.org/10.1061/(asce)0733-9399(1996)122:5(482)

Yoo CH, Fehrenbach JP (1981) Natural frequencies of curved girders. J Eng Mech Div 107:339–354

Yoon KY, Park NH, Choi YJ, Kang YJ (2006) Natural frequencies of thin-walled curved beams. Finite Elem Anal Des 42:1176–1186. https://doi.org/10.1016/j.finel.2006.05.002